Anomalously silver-rich vein-hosted mineralisation in disseminated-style gold deposits, Jiaodong gold district, China

Stephanie E. Mills [a],[*], Andrew G. Tomkins [a], Roberto F. Weinberg [a], Hong-Rui Fan [b]

[a] School of Geosciences, Monash University, Melbourne, Australia
[b] Institute of Geology and Geophysics, Chinese Academy of Sciences, Beijing, China

A B S T R A C T

Structural measurements and geochemical analyses, including bulk and in situ pyrite geochemistry, sulfur isotopes, and whole-rock geochemistry, are presented for the No. 3 orebody of the Jiaojia gold deposit (JJ3), located in the Jiaodong district of northeast China. The JJ3 orebody is distinct from the main orebody of the Jiaojia deposit (JJ1) because it is characterised by steeply dipping sub-metric quartz-pyrite veins with up to 300 ppm of gold, whereas the JJ1 orebody represents an archetypal example of the disseminated and veinlet style mineralisation characteristic of regional faults in the Jiaodong district. Measurements on JJ3 veins and the host Jiaojia-Xincheng regional fault are consistent with development of mineralised, steeply dipping extension fractures during normal faulting, which produced the fault-hosted disseminated-style JJ1 orebody. Trace element geochemistry of pyrite in these veins shows that JJ3 pyrite is geochemically distinct from those of the main Jiaojia and Xincheng orebodies, being relatively enriched in Ag and Pb, as well as Ba, Bi, Te and Au, and relatively depleted in Cu and As. Enrichment in Ag and Pb is possibly related to infiltration of a saline hydrothermal fluid, as both are effectively transported as chloride complexes; however, depletion of Cu, which is also mobile as chloride complexes, requires a low temperature saline fluid where Cu is no longer soluble. The textural setting of the ore minerals suggests that these cooler fluids likely infiltrated during the waning stages of the hydrothermal system. The relative abundance of barite in the JJ3 orebody, which formed from late-stage oxidised magmatic–hydrothermal fluids, also supports the interpretation that the JJ3 orebody represents a late mineralisation event. The pervasive alteration surrounding the JJ3 orebody is K-feldspathic with a minor sericitic overprint, indicating an earlier higher temperature pervasive fluid flow event that was followed by low-temperature mineralising fluids. This interpretation implies that fracture dilation post-dated the earliest alteration, and that mineralisation and pervasive alteration in the JJ3 orebody are geochemically disconnected. Thus structural analysis is expected to be the most effective targeting method in future exploration for similar ore bodies.

1. Introduction

Located in the northeast Shandong Province, the Jiaodong gold district is responsible for more than 25% of China's annual gold production, at a time when China is the world leader in gold production (Goldfarb et al., 2014). Given that the Jiaodong district covers only ~20,000 km^2 (representing 0.2% of China's land area) and yet hosts 30% of China's total gold reserves (Guo et al., 2013), this region is one of the most important gold producing regions globally and has been the focus of much modern research (e.g. Li et al., 2015; Song et al., 2015; Q. Yang et al., 2014). Within the district, over 95% of mineralisation is hosted in Mesozoic granitoids, which intrude Archean and Proterozoic cratonic basement of the North China Craton (Qiu et al., 2002).

Among the gold deposits in the Jiaodong district, there are two world-class gold fields, the Jiaojia-Xincheng and the Linglong fields, each containing over 150 t of Au (Qiu et al., 2002; C. Wang et al, 2015). The Jiaojia-Xincheng and Linglong fields contain many individual deposits within broader areas of related mineralisation. These two gold fields, in addition to being the largest gold concentrations in the Jiaodong district, are considered to be the archetypal examples of the two most common styles of mineralisation in the Jiaodong district. 'Jiaojia-style' mineralisation is typified by disseminated and veinlet mineralisation forming tabular orebodies in the brecciated footwall of regional faults (Fan et al., 2007; Qiu et al., 2002). 'Linglong-style' mineralisation is characterised by centimetre to metre wide quartz-pyrite veins (lodes) developed along subsidiary fracture networks associated with regional faults (Fan et al., 2007; Qiu et al., 2002). Although distinguishing between these main styles of mineralisation can be helpful for a brief description, presenting 'Jiaojia-' and 'Linglong-styles' as endmember mineralisation styles indicates they are exclusive to

* Corresponding author at: School of Geosciences, Bldg. 28, Monash University, Clayton VIC 3800, Australia. Tel.: +61 4 3959 3245.
  E-mail address: stephanie.mills@monash.edu (S.E. Mills).

one another, while in fact both styles can be locally important within a single deposit.

In this study, we show that steeply dipping quartz-pyrite veins, a similar structural style of mineralisation to that found in the Linglong gold field, are an important feature of the Jiaojia-Xincheng gold field. They contain geochemical anomalies that, when combined with an analysis of the structural setting, provide insights into variations in the evolution of the hydrothermal fluids that formed the world-class Jiaojia-Xincheng gold field.

2. Jiaojia-Xincheng gold field

2.1. Regional geology

The Jiaodong gold district is located on the eastern margin of the North China Craton, which has experienced multiple significant Phanerozoic reactivations since cratonisation at 1.8 Ga. One of the most unique aspects of the North China Craton is that it represents the best known example worldwide of a craton that has become 'decratonised' through destruction of its stabilising lithospheric keel (Griffin et al., 1998). The destruction of the sub-continental lithospheric mantle (SCLM) took place mainly during the Cretaceous and was limited to the eastern portion of the craton, with some areas losing up to 100 km of lithospheric root (Griffin et al., 1998; Zhu et al., 2012). This drastic thinning of the lithosphere occurred coevally with extensional tectonics, mantle upwelling, widespread magmatism, and development of gold mineralisation along the margins of the eastern North China Craton (Li et al., 2012; Wu et al., 2005).

In addition to loss of lithosphere, all margins of the North China Craton experienced significant orogenesis during the late Paleozoic to Mesozoic. Of particular importance to the basement architecture of the Jiaodong district was the Triassic (~240 Ma) continental collision

between the southern margin of the North China Craton and the Yangtze Craton, which saw continental material from the Yangtze craton subducted beneath the North China Craton (Hacker et al., 2006). The collision also resulted in formation of the Sulu ultrahigh pressure (UHP) terrane, which forms the basement of the eastern Jiaodong district. Subduction of the Pacific Plate beneath the margin of east Asia was also initiated in the Cretaceous, and is commonly suggested to have been a far-field control on lithospheric destruction and consequent processes (e.g. Goldfarb et al., 2014). The Tan Lu fault zone, which is a regional transcrustal fault that parallels the eastern margin of the North China Craton, was also active during the Cretaceous and has been shown to be a corridor for mantle upwelling (Guo et al., 2013; Xiao et al., 2010). The Tan Lu fault is located only ~30 km from the westernmost extent of the Jiaodong district (Fig. 1).

The basement of the Jiaodong district is comprised of two terranes: 1) the aforementioned Sulu UHP terrane in the east, typically considered to bear affinity to the Yangtze Craton, and 2) the Archean to Paleoproterozoic Jiaobei terrane in the west, which is part of the North China Craton (Jahn et al., 2008; Tang et al., 2008; Fig. 1). The two terranes are separated by the Wulian-Yantai fault. There is no evidence for the existence of Paleozoic to middle Jurassic aged rocks in the Jiaodong district, likely indicating intensive uplift and erosion during this period (Guo et al., 2013). The earliest preserved units deposited after cratonisation are late Cretaceous volcano-sedimentary sequences hosted in the Jiaolai basin, which opened as a result of extensional tectonics (L. Zhang et al., 2003). These rocks are distributed throughout the southern portion of the Jiaodong district.

Despite the lack of Paleozoic and early Mesozoic strata, intrusive magmatism was active starting in the Jurassic. Magmatism in the Jiaodong district is typically divided into Jurassic, early Cretaceous, and late Cretaceous periods. Magmatism in the Jurassic was active at ~160 Ma and resulted in the Linglong, Luanjiahe, and Kunyushan
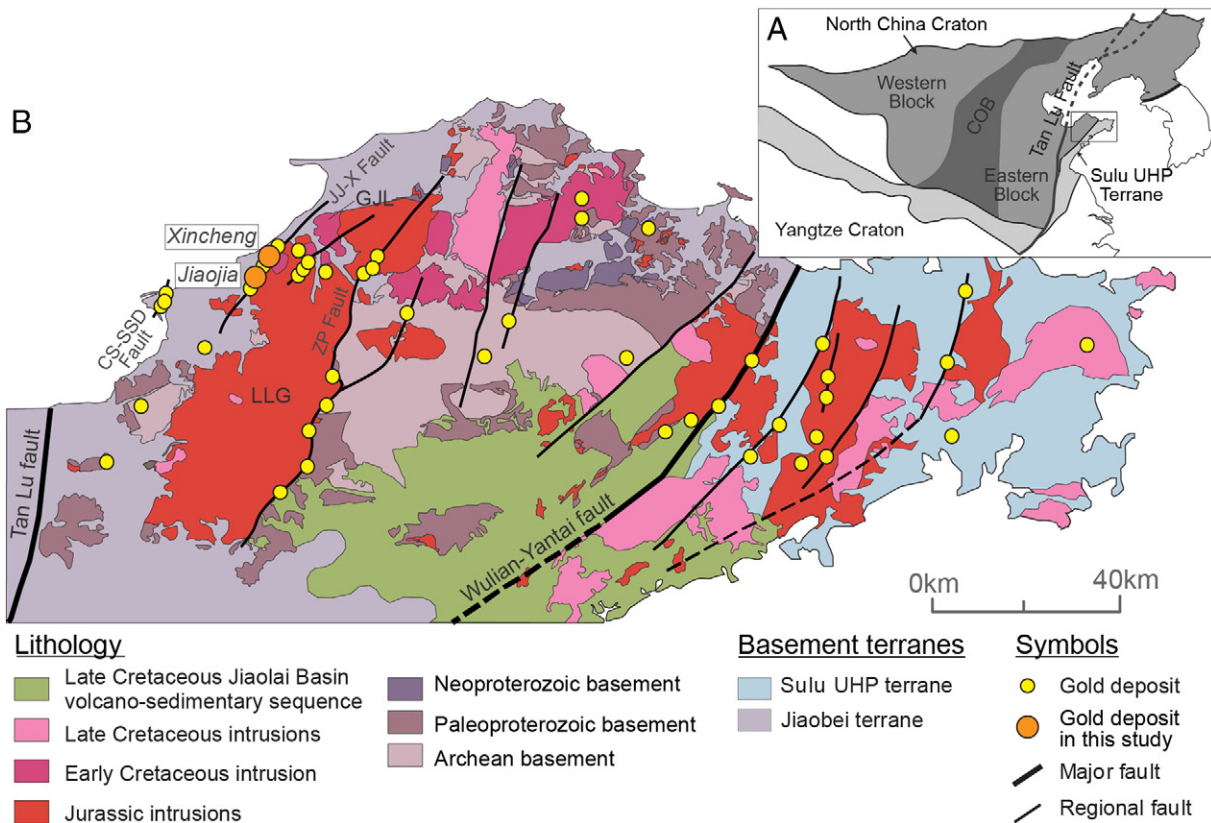
Fig. 1. (A) Regional map of the North China Craton, and (B) geologic map of the Jiaodong gold district. Major gold mineralisation belts and the deposits sampled for and referred to in this study are indicated (after Fan et al., 2003; Goss et al., 2010; Hacker et al., 2006; Li et al., 2012; Liu et al., 2013; Zhang et al., 2010; Yang et al., 2012). JJ-X fault = Jiaojia-Xincheng fault, CS-SSD fault = Cangshang-Sanshandao fault, ZP fault = Zhaoping fault, LLG = Linglong granite, GJL = Guojialing granodiorite.

granites (Hou et al., 2007; Yang et al., 2012). Early Cretaceous magmatism peaked around 125 Ma and resulted in the Guojialing granodiorite. Late Cretaceous magmatism, typically ~115 Ma, resulted in the Aishan and Sanfoshan granites as well as widespread intrusion of mafic dikes (Cai et al., 2013; Charles et al., 2011a; Goss et al., 2010; Yang et al., 2012). Mineralisation across the district formed in a relatively constrained pulse around 120 ± 5 Ma (Li et al., 2003; Wang et al., 1998; C. Wang et al., 2015; X.O. Zhang et al., 2003). Gold is hosted along a series of regional NE striking faults, which either follow the contacts of Mesozoic intrusions or, less commonly, cross-cut the intrusions, such that >95% of mineralisation is intrusion-hosted (Qiu et al., 2002).

2.2. Deposit description

The Jiaojia-Xincheng gold field is located along the Jiaojia-Xincheng (JJ-X) fault, which follows the western contact of the Linglong granite where it is juxtaposed with Archean basement and Guojialing granodiorite (Fig. 2). Although other deposits are often included in the Jiaojia-Xincheng field, for this study we focus on the Jiaojia and Xincheng deposits as these are the archetypal and largest examples of the disseminated style of mineralisation. The Xincheng deposit is located ~5 km north of the Jiaojia deposit, with both located at bends in the NW dipping JJ-X fault where the strike locally changes by ~30°: from ENE to NNE for Jiaojia, and from NNE to ENE for Xincheng.

The Jiaojia deposit is hosted where Archean basement is faulted against the Linglong granite, with mineralisation hosted in the footwall of the fault in brecciated Linglong granite. The Xincheng deposit is located at the contact between the Linglong granite (hanging wall) and Guojialing granodiorite (footwall) with mineralisation hosted in the Guojialing granodiorite. Brecciation in all footwall units along the JJ-X fault is extreme and is commonly referred to as cataclastic, with conflicting reports over the existence and degree of ductile deformation present

(Lu et al., 2007; Qiu et al., 2002). The fault plane in both deposits is well-developed, forming a sharp planar surface (e.g. Fig. 5B). A layer of fault gouge up to 50 cm thick occurs along the fault plane, above the brecciated footwall. Pervasive brecciation extends up to 2 m (referred to as the 'brecciation zone') before transitioning to a much wider zone of extensive fracturing where original magmatic fabrics are still intact, with the degree of fracturing decreasing with distance from the fault.

Disseminated mineralisation is mainly developed in the most brecciated and fractured portions of the deposit, transitioning to veinlet style mineralisation as the degree of brittle deformation decreases. There are also mineralisation style variations with depth: for example, in the Xincheng deposit, shallower levels are characterised by disseminated style mineralisation, whereas at deeper levels anastomosing veinlet networks prevail.

The combined disseminated and veinlet mineralisations form tabular orebodies broadly parallel to the JJ-X fault that can extend out up to 50 m from the fault (referred to as the 'middle zone'). This is the main style of mineralisation in both the Jiaojia and Xincheng deposits, and for simplicity these orebodies are referred to here as the JJ1 and X1 orebodies for Jiaojia and Xincheng, respectively (Fig. 2). Barren alteration halos in both Jiaojia and Xincheng can extend for hundreds of metres away from the fault (referred to as the 'outer zone').

In addition to the main JJ1 and X1 disseminated orebodies, the Jiaojia deposit hosts an additional orebody located 50–300 m away from the JJ-X fault, which is the focus of this study. In this additional orebody, mineralisation is hosted in steeply dipping fractures as quartz-pyrite veins of the typical 'Linglong style' mineralisation, ranging from small veins in anastomosing networks to larger, sub-metre veins. These veins locally contain up to 300 ppm Au and comprise the No. 3 orebody at Jiaojia, and are thus referred to as the JJ3 orebody in this paper (Fig. 2). The JJ3 orebody veins vary slightly in strike and dip, but can be generally described as NE–SW striking and dipping at a high angle towards either
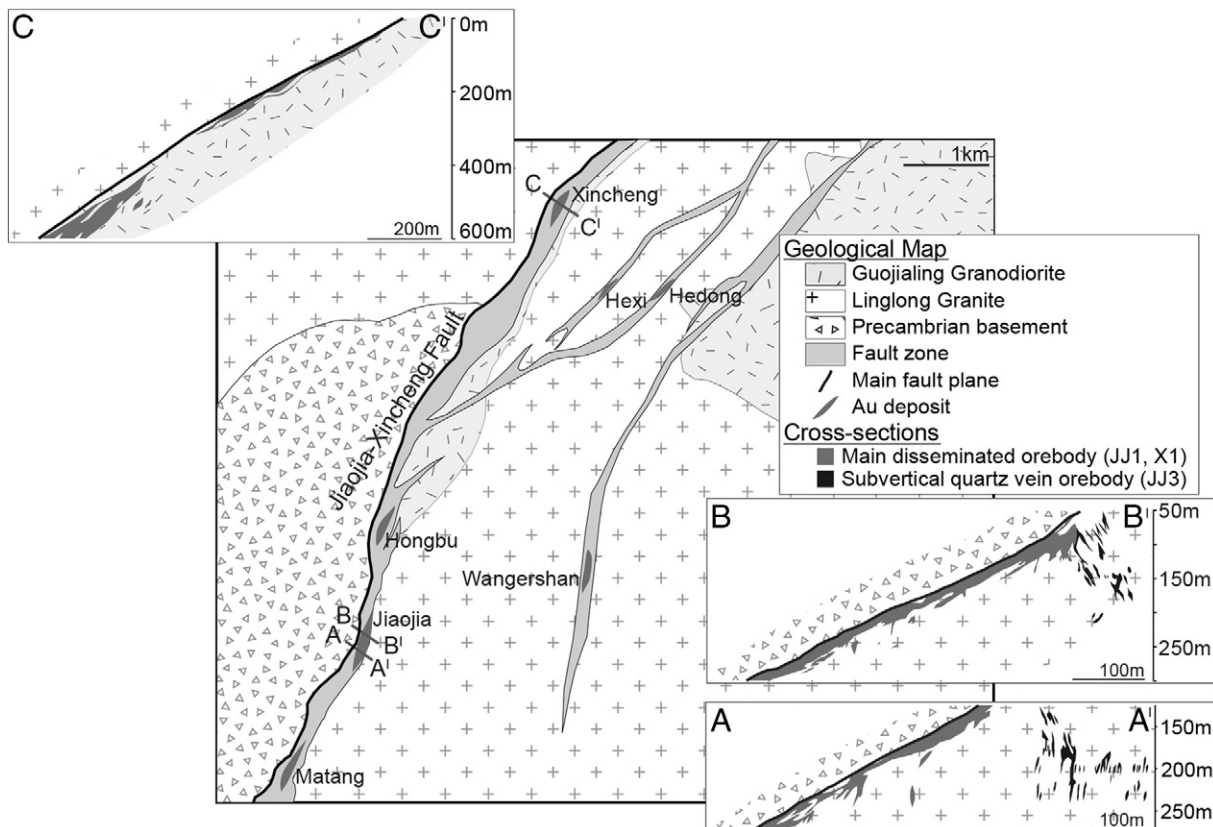
Fig. 2. Gold field-scale map of the Jiaojia-Xincheng camp, after Qiu et al. (2002). A to A[I] cross-section represents the Jiaojia No. 102 line, B to B[I] represents the Jiaojia No. 114 line, and C to C[I] represents the Xincheng No. 175 line.

the NW or SE, making them parallel in strike to the NW-dipping JJ-X fault but dipping more steeply or in the opposite direction. Currently, this ore resource is only being developed in the Jiaojia deposit, though recent drilling has confirmed the presence of similar mineralisation in the Xincheng deposit. In the Jiaojia deposit, the JJ3 orebody is only mined to a depth of 250 m, whereas the JJ1 orebody extends to >700 m depth.

3. Physical characteristics of the JJ3 orebody

3.1. Petrography

Disseminated mineralisation in the JJ1 and X1 orebodies is characterised by pyrite, with secondary galena, chalcopyrite, and sphalerite disseminated through an intensely brecciated wall rock (Fig. 3A).
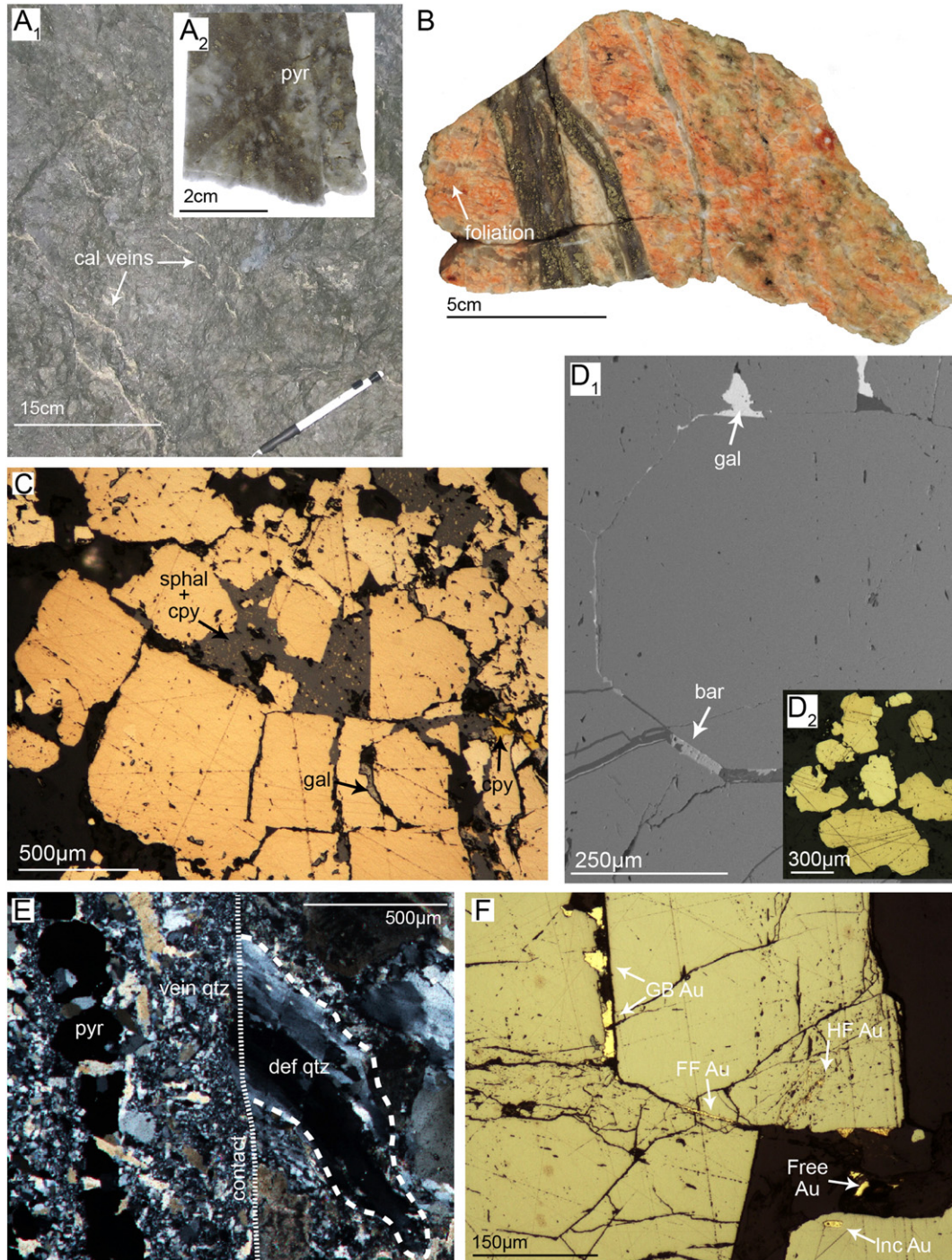
Fig. 3. Examples of mineralisation in the Jiaojia-Xincheng camp. (A_1) Photograph of brecciated zone (X1 orebody) with late white calcite veins (cal veins) and disseminated pyrite mineralisation (A_2). (B) Photograph of high grade JJ3 pyrite vein in red-stained alteration, averaging 300 ppm Au. (C) Reflected light photomicrograph of angular pyrite crystals in JJ1 with minor chalcopyrite (cpy), galena (gal), and sphalerite (spahl). (D) SEM BSE image of fractured JJ3 pyrite (pyr) with galena (gal) and barite (bar) in fractures. (D_2) Reflected light photomicrograph of rounded pyrite crystals in JJ3 samples. (E) Transmitted light cross-polars photomicrograph of the margin of a hydrothermal vein in a JJ3 sample. The contact between vein and host rock is defined by the stippled line. To the right of the vein margin, a large deformed grain of quartz (def qtz) in the Linglong granite, outlined with dashed lines, is truncated against the vein margin. Within the vein (to the left of the contact) hydrothermal quartz (vein qtz) is fine-grained and undeformed. (F) Reflected light photomicrograph of gold grains in JJ3 pyrites, forming as grain-boundary gold (GB Au), fracture-fill gold (FF Au), healed fracture gold (HF Au), free grains of gold, and gold formed as inclusions (Inc Au).

Pyrite forms as either large discrete crystals or as clusters of smaller crystals, which are generally cubic in both cases. Veinlet mineralisation is texturally very similar, with veinlets typically containing very little or no quartz and large pyrite crystals. Detailed petrographic descriptions and paragenetic interpretation of mineralisation in the JJ1 and X1 orebodies are described in Mills et al. (in review-a).

Mineralisation in the JJ3 orebody is made up of steeply dipping veinlets and veins (Fig. 3B) that often contain more quartz than is common in the JJ1 orebody (~70% vs. ~30%) but less than is observed in 'Linglong style' deposits (often >85%). Pyrite is by far the most common sulfide mineral, a characteristic common to all deposits within the Jiaodong district. Pyrite crystals in the JJ3 orebody typically have a slightly more rounded morphology and contain fewer inclusions than is typical for JJ1 and X1 pyrites (Fig. 3C, D). Although galena and barite are present in higher quantities than typical of the JJ1 and X1 orebodies, very little sphalerite and almost no chalcopyrite is observed (Fig. 3C, D). The main gangue mineral in JJ3 veins is quartz, but fractures in pyrite are commonly filled with fine grained sericite, and occasionally carbonate minerals such as ankerite. Quartz in the JJ3 veins is extremely fine grained and exhibits only minor deformation compared to quartz grains in the host granite, which define a distinct ductile foliation together with oriented micas (Fig. 3E).

Visible gold grains in the JJ3 orebodies occur in the same fashion as in JJ1 and X1, forming primarily within pyrite fractures, but also along pyrite grain boundaries and occasionally as free gold grains in quartz (Fig. 3F). In a study by Yang et al. (2011) 62% of observed gold grains from the Jiaojia deposit were hosted by pyrite, with 13.5% hosted by chalcopyrite, negligible gold hosted by galena and sphalerite, and most of the remainder hosted by vein quartz. From the gold grains observed in this study and observed in Mills et al. (in review-a), which also included results from the Xincheng and the Linglong deposits, over 90% of gold grains were hosted by pyrite.

SEM observations and EDS analyses indicate that gold occurs as electrum, containing between 25 and 40% Ag, averaging ~35%. This is a slightly higher Ag content than electrum in JJ1 and X1, which also typically contains ~30% Ag. Similar to JJ1 and X1, JJ3 pyrite grains contain telluride and sulfosalt mineral inclusions, though in far lower abundance and diversity than the main orebodies. The most common mineral in the JJ3 orebody aside from pyrite is galena, which can contain several wt.% Ag, followed by barite, which occurs as discrete crystals in the silicate matrix and rarely in pyrite fractures with galena. The galena crystals in the JJ3 orebodies contain 2–3 wt.% more Ag on average than galena from the JJ1 and X1 orebodies. Barite is significantly more abundant in the JJ3 orebody, whereas chalcopyrite and sphalerite are virtually absent. Hessite is the most common telluride; no Au–Ag telluride minerals such as petzite or sylvanite were observed. Tellurobismuthite is rare, as are minerals in the Bi–Ag–Pb sulfide solid solution.

Alteration in the Jiaojia-Xincheng field, and in the broader Jiaodong district, is potassic in nature. In the Jiaojia and Xincheng deposits, alteration is zoned and generally mimics the deformation zones. In the brecciated zone, alteration consists of pervasive fine-grained sericite and silicification with very little evidence of original magmatic clasts (Fig. 3A). Hand samples of this brecciated zone are typically grey and can contain late calcite veins cross-cutting earlier alteration, which are often themselves fractured or brecciated. In the middle zone, alteration remains dominantly sericitic, with sericite preferentially altering plagioclase cores and forming along fractures and twinning planes (Fig. 4A). Original magmatic K-feldspar crystals often exhibit no alteration, even when all plagioclase is heavily sericitised (Fig. 4B). In the distal part of the middle zone, early K-feldspar alteration is evidenced by partially altered plagioclase crystals. The K-feldspar alteration is initially developed in the centre of the plagioclase crystals, where K-feldspar forms in hazy patches and obscures original plagioclase twinning (Fig. 4C, D). This K-feldspar alteration is overprinted by sericitic alteration, with more intense sericitisation closer to the JJ-X fault. K-feldspathisation with variable sericitic overprint is present in the outer zone as well, although here alteration transitions from pervasive to fracture-controlled.

The middle and outer zones commonly exhibit an intense red staining associated with alteration (Fig. 4E), which is a distinct characteristic of many deposits in the Jiaodong district. This red staining is likely the result of disseminated hematite nanoparticles in feldspar crystals (Putnis et al., 2007) and is typically associated with early K-feldspar alteration. Magmatic biotite is consistently absent in altered rocks but at the alteration front in fresh granite biotite can be observed altering to sericite (Fig. 4E). It is possible that the alteration of magmatic biotite to sericite and resulting liberation of iron was a contributing factor to development of the red staining accompanying early stages of alteration. At the very distal edges of the alteration halo, plagioclase crystals are often 'bleached', whereby they become white and porous (Fig. 4F). SEM observations and EDS analyses indicate that these crystals have been stripped of any major cations (Ca, Na, K) and are reduced to an aluminosilicate skeleton (Fig. 4F). It is unclear the process by which this occurs, however as this is the most distal alteration observed it is possible that the K source in early altering fluids was exhausted prior to alteration at the distal fringes, such that high temperature and relatively acidic fluids removed existing Na cations but did not replace them with K.

Alteration in the JJ3 orebody reflects the location of these orebodies in the middle to outer zones. Alteration is pervasive, with particularly intense red staining, and is primarily K-feldspar alteration with minor to intermediate degrees of overprinting sericite. There is a sharp contact between mineralised veins and the host rock, and there has been no observation of preferential alteration in the host rocks proximal to ore veins.

3.2. Structural setting

The 'Jiaojia- and 'Linglong-styles' of mineralisation have been previously suggested to exist on a structural continuum. Lu et al. (2007) attributed the variations in mineralisation style to differences in depth, with the 'Jiaojia-style' reflecting deeper levels and the 'Linglong-style' characterising shallower levels. In contrast, Qiu et al. (2002) concluded that the differences are the result of variation in the degree of deformation in the host rock. In the Qiu et al. (2002) model, larger structures such as regional faults that focus deformation are more favourable for 'Jiaojia-style' mineralisation, whereas strain decreases with distance from the large structures and favours the development of discrete fractures (hence, 'Linglong-style' mineralisation). The transition between the two is characterised by anastomosing veinlet networks. In a situation like the Jiaojia deposit, all styles of mineralisation (disseminated, veinlet, and quartz veins) are present at roughly equal depths, so the argument of Lu et al. (2007) does not appear valid. It appears more likely that the variation in mineralisation is related to previous deformation of host rock with influence from other factors such as fluid pressure, the orientation and magnitude of stress, and changes in host rock rheology due to metasomatism.

Despite considerable debate on the structural evolution of the Jiaodong district prior to mineralisation, it is generally agreed that mineralisation took place during extensional tectonics such that pre-existing fault planes experienced normal movement (Charles et al., 2011b; Lu et al., 2007; Qiu et al., 2002). As can be seen in Fig. 5, fractures in the JJ3 orebody are broadly NE–SW striking with steep dips to the NW or SE. Measurements from the JJ-X fault are likewise NE–SW striking with dips between 30 and 50° to the NW. In a previous study by Charles et al. (2011b), measurements of fault planes from microtectonic sites were taken from the region around the JJ-X fault. Sites in both the Linglong granite and the Guojialing granodiorite were measured, and results strongly indicated a NW–SE extensional event. The maximum stress axis was interpreted to be subvertical and subhorizontal for the minimum stress axis, indicative of normal faulting (Charles et al., 2011b). The results also illustrated that a well-distributed penetrative fault network disrupts the Linglong and Guojialing intrusions. The measurements presented in this study (Fig. 5) illustrating the steeply dipping nature of the JJ3 veins combined with the regional study by
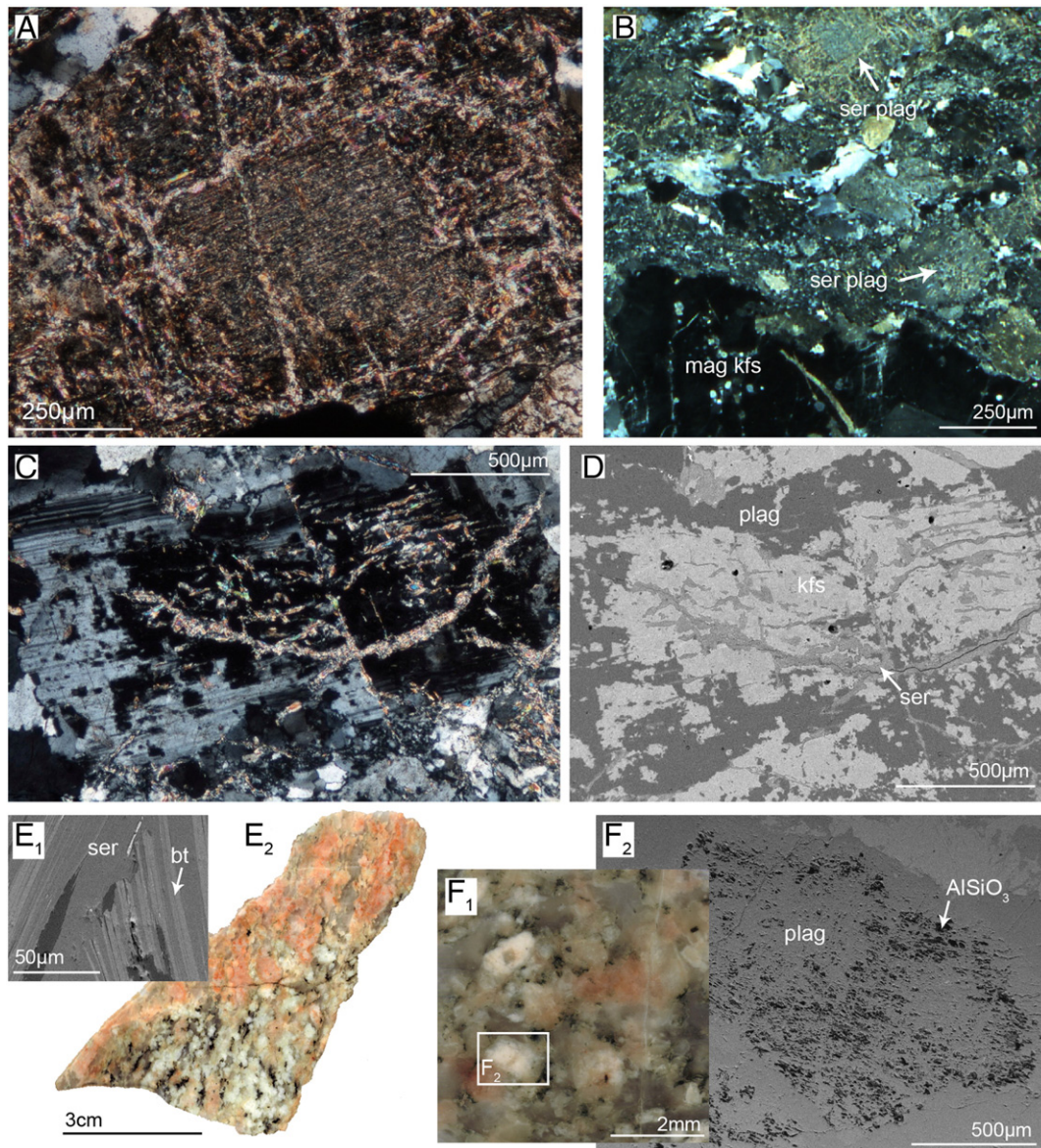
Fig. 4. Examples of alteration in the Jiaojia-Xincheng camp. (A) Transmitted light cross-polars photomicrograph of a sericitised plagioclase crystal, with the most intense sericitisation in the centre of the crystal, mainly following twinning planes, and also coarser sericite forming at the edges and along fractures. (B) Transmitted light cross-polars photomicrograph of an unaltered magmatic K-feldspar megacryst (mag kfs) surrounded by sericitised plagioclase crystals (ser plag). (C) Transmitted light cross-polars photomicrograph of an original magmatic plagioclase crystal with altered, cloudy centre and sericite growing along fractures and twinning planes, also focused in the centre of the crystal. (D) SEM BSE image of the same grain as (C) showing that the outer crystal where twinning is still visible is plagioclase (plag), and the interior of the crystal that has become cloudy is altered to K-feldspar (kfs), which is then overprinted by the sericitic alteration (ser). (E_1) SEM BSE image of original magmatic bladed biotite crystals (lighter gray 'bt') altering to sericite (darker gray 'ser'). (E_2) Hand sample showing the transition from unaltered, biotite-bearing Linglong granite to red-stained, K-feldspar altered (biotite-absent) granite. (F_1) Hand sample illustrating the bleached nature of plagioclase in the most distal alteration zone. (F_2) SEM BSE image of crystal outlined in (F_1) showing that the bleached plagioclase crystal has become porous, with the darker holes representing aluminosilicate skeleton stripped of cations.

Charles et al. (2013) suggest it is likely that the JJ3 orebody developed during normal faulting, and that mineralisation is hosted in extension-related veins. These conclusions are in good agreement with previous studies, which suggested that the JJ3 orebody and the steeply dipping veins resulted from normal movement (Lu et al., 2007; Qiu et al., 2002).

4. Geochemistry of the JJ3 orebody

4.1. Pyrite geochemistry

4.1.1. Methods

Pyrite geochemistry from JJ3 samples was conducted by both bulk and in situ methods. The combination of bulk and in situ analyses is intended to provide a robust consideration and comparison of overall

pyrite geochemistry while still considering specific aspects of how different elements are hosted within pyrite. The bulk geochemistry results have been previously presented in Mills et al. (in review-b); however, that study made no distinction between the orebodies within the Jiaojia deposit as the focus was a comparison between the Zhao-Ye and Muru mineralisation belts. Despite broad similarities in the mineralogy JJ1/X1 orebodies and the JJ3 orebody, we investigated the chemical nature of pyrite, by far the most dominant sulfide in all orebodies, for variations in geochemistry as a function of mineralisation style for the first time. Bulk pyrite geochemistry analysis was conducted on 11 samples from the JJ1 orebody, 13 samples from the X1 orebody, and 6 samples from the JJ3 orebody. Whole rock samples were coarse-crushed in ceramic jaw crushers. Pyrite crystals were picked by hand to ensure that analyses reflected only the geochemistry of pyrite and inclusions in pyrite. Pyrite
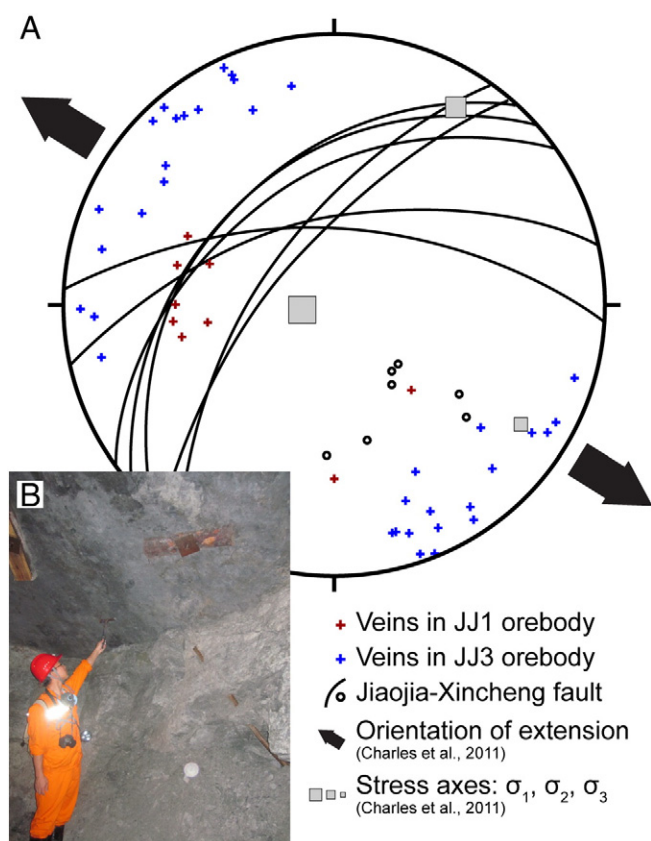
Fig. 5. (A) Stereonet of measurements of quartz-pyrite veins (<1 cm to >30 cm in width) from the JJ1 and JJ3 orebodies (poles to plane) and measurements from the JJ-X fault (plane and pole to plane), combined with the orientation of the regional extensional event and stress axes determined in Charles et al. (2011b). Note that over 70% of JJ3 measurements are dipping over 75°. (B) Field picture of the JJ-X fault, showing the sharp nature of the fault plane.

separates were crushed in an agate mortar and pestle to a homogenised powder. Silver, As, Bi, Co, Cu, Mo, Ni, Pb, Sb, Se, Sn, Te, W and Zn were analysed by ICP-AES and ICP-MS following a digestion by perchloric, nitric and hydrofluoric acids and leaching by dilute hydrochloric acid. Gold analysis was done by atomic absorption spectroscopy (AAS) on a precious metal bead produced from a separate of the homogenised pyrite powder. Analyses were completed by ALS Laboratories, and the precision of data was not reported. Where elements were below detection, half the detection-limit is used.

In situ analyses of single pyrite crystals were done by LA-ICP-MS transects across pyrite crystals in polished blocks. Two samples from the JJ3 ore body were selected, with three crystals in each sample analysed. The analyses were carried out using a New Wave UP 213 nm N:YAG laser ablation microprobe coupled with a Thermo Finnigan X series II, quadrupole ICP-MS at the School of Geosciences, Monash University. Analyses were in helium atmosphere, employing a pulse rate of 5 Hz and beam energy of ~5.5–6.5 J/cm^2 at the sample. Laser spot size was 80 μm in diameter, with a 10 μm s − 1 dwell rate along transect lines. NIST 610 glass was used as a reference material for standardisation prior to, during, and after analyses and was used to correct for instrument drift throughout analyses. Elements analysed were ^{29}Si, ^{33}S, ^{57}Fe, ^{59}Co, ^{61}Ni, ^{63}Cu, ^{67}Zn, ^{75}As, ^{77}Se, ^{95}Mo, ^{107}Ag, ^{118}Sn, ^{121}Sb, ^{125}Te, ^{182}W, ^{197}Au, ^{208}Pb and ^{209}Bi. Analyses were measured as relative concentrations in counts per second (cps), as there was no calibrated sulfide standard available; however, the relative elemental trends reflected in the analyses are expected to be valid and thus can be used qualitatively and semi-quantitatively.

Sulfur isotope analyses were conducted on 9 JJ1 samples, 14 X1 samples, and 6 JJ3 samples. Analyses were conducted at Monash University.

A fine-crushed separate of the pyrite sample separated from whole rock was loaded in a tin cup with vanadium pentoxide and combusted to SO_2 in a Carlo Erba 1110 Flash EA, with δ^{34}S values measured using a mixed continuous flow − dual inlet set up with a Thermo Delta Advantage Isotope Ratio Mass Spectrometer. Standardisation of δ^{34}S to the CDT scale was via analysis of the International Standard NBS-127. During the course of analyses the International Standard NBS 123 Balmain sphalerite was analysed every 5 samples and yielded a standard deviation over 4 days of analyses of 0.24‰.

4.1.2. Bulk pyrite geochemistry

The bulk pyrite geochemistry results are given in Table 1. Figure 6 shows that the JJ3 orebody has distinct differences in bulk pyrite geochemistry compared to the JJ1 and X1 orebodies. Pyrites from the JJ3 orebody are the most enriched in Pb and Ag, with moderate enrichments in Ba, Bi, and Te. Additionally, the average Au concentration for JJ3 pyrite separates is slightly higher than that of JJ1 (178 ppm versus 128 ppm, respectively) but is lower than the average value of 253 ppm for X1 (Fig. 6). The average Au results from X1 are skewed by a single outlier sample that is an order of magnitude higher than any other sample in this study (an outlier is defined as values greater than $1.5 \times$ the interquartile range; see Fig. 6 caption). Without the high Au outlier, the average Au concentration for the X1 orebody is 45 ppm, less than half the average of the JJ3 orebody. Outlier skewing may also have a minor effect on the comparison of Au between JJ1 and JJ3 because, despite the higher average value in JJ3, a plot of Au versus Ag (Fig. 7A) illustrates that the higher JJ3 average is likely due to a single high value in the JJ3 results, whereas the remainder of the JJ1 and JJ3 results are comparable. Thus, JJ3 is moderately enriched in Au compared to X1 and comparable to Au concentrations in JJ1.

Pyrites from the JJ3 orebody have very low concentrations of Sb and Mo, lower even than those in JJ1 and X1 where averages are typically <1 ppm. Arsenic and Cu also have significantly lower average concentrations in JJ3 pyrites (Fig. 6). The JJ1 and X1 pyrites already have extremely low As concentrations (average ~100 ppm) when compared to pyrites from typical orogenic deposits (100's–1000's of ppm; Large et al., 2009), and there is 5 times less As in the JJ3 pyrites than in the JJ1 and X1 pyrites. Pyrites from the JJ3 orebody average only 20 ppm As, with a maximum value of 45 ppm, which is well shy of the ~100 ppm average values in JJ1 and X1. The difference in Cu concentrations is also distinct as the JJ3 orebody has negligible amounts of Cu present, averaging only 15 ppm, whereas the averages for the JJ1 and X1 orebodies are 602 and 350 ppm, respectively. Again, the X1 results are skewed by a single outlier value for that data set, which when removed results in only ~30 ppm average Cu. The 602 ppm average for JJ1 is representative of the data. The bulk pyrite results are also in good agreement with petrographic observations from JJ3, which indicate that significant argentiferous galena and barite occur in or on pyrite, whereas other base metal sulfide minerals, particularly chalcopyrite, are relatively lacking.

The JJ3 orebody is the only orebody in the Jiaojia, Xincheng, Jiuqu, Sanjia, Denggezhuang, and Jinqingding deposits (Mills et al., in review-b) that has a negative correlation between Au and Ag (Fig. 7A). This contrasts with the distinct positive Au–Ag correlation that is evident in bulk and in situ pyrite geochemistry for the X1 and JJ1 orebodies, noted in Mills et al. (in review-b) as one of the most defining features of these orebodies. Therefore, it is of particular interest that not only are the JJ3 samples enriched significantly in Ag with respect to other orebodies in the region, but also that they have a distinct, fairly well developed negative correlation with Au. Due to the close association between Ag, Te, Bi, and Pb, these elements also all exhibit a similar negative correlation with Au while having a strong positive correlation with one another (Fig. 7A–D). There is no apparent correlation between Au and either As or Cu for JJ3 (Fig. 7E, F).

It is possible that the negative Au–Ag correlation and apparent enrichment of Ag and Pb in the JJ3 orebody could be due to contamination

Table 1
Bulk pyrite geochemistry of the JJ1, JJ3 and X1 orebodies.

Sample	Deposit	Orebody	Ag	As	Au	Bi	Co	Cu	Mo	Ni	Pb	Sb	Se	Sn	Te	W	Zn
Unit			ppm	ppm	ppm	ppm	ppm	ppm	ppm	ppm	ppm	ppm	ppm	ppm	ppm	ppm	ppm
Detection limit			0.01	0.2	0.01	0.01	0.1	0.2	0.05	0.2	0.5	0.05	1	0.2	0.05	0.1	2
14_1	Jiaojia	JJ1	220.00	90.4	142.70	155.50	106.0	280.0	1.43	31.5	2450.0	4.12	2	0.4	129.00	20.4	96
43_2	Jiaojia	JJ1	63.70	49.4	16.30	50.20	39.8	29.3	0.09	32.0	383.0	0.14	4	0.1	37.70	0.4	4
44_1	Jiaojia	JJ1	347.00	31.2	351.00	164.00	23.2	22.0	0.06	29.8	1420.0	0.15	4	0.1	206.00	0.1	6
49_4	Jiaojia	JJ1	15.75	336.0	38.50	9.29	14.2	23.2	0.19	5.7	565.0	1.37	2	0.1	8.24	2.0	1
49_5	Jiaojia	JJ1	89.00	57.1	74.20	27.70	6.4	78.7	0.07	4.3	3770.0	1.15	4	0.2	18.70	1.4	1
51_6	Jiaojia	JJ1	140.00	164.5	85.90	159.50	7.9	3050.0	0.30	1.5	8010.0	2.20	1	0.1	17.95	0.5	2220
51_7	Jiaojia	JJ1	39.50	99.7	21.30	54.10	5.4	1910.0	2.29	2.2	1410.0	2.67	1	0.2	5.56	0.7	300
78_1_2	Jiaojia	JJ1	71.70	11.2	154.00	375.00	14.4	12.8	0.08	14.5	559.0	0.13	5	0.1	255.00	0.2	1
78_2	Jiaojia	JJ1	234.00	15.3	269.00	143.50	21.5	9.4	0.10	23.2	1090.0	0.13	6	0.1	121.00	0.2	2
79_1	Jiaojia	JJ1	233.00	242.0	93.60	433.00	10.6	2380.0	0.24	2.0	1490.0	0.44	1	0.1	0.65	0.1	61
79_2	Jiaojia	JJ1	20.30	264.0	17.50	50.40	6.0	997.0	0.26	5.1	253.0	0.21	1	0.1	0.30	0.1	58
50_1	Jiaojia	JJ3	930.00	14.9	20.30	460.00	20.6	21.2	0.14	65.7	9550.0	0.09	3	0.1	460.00	6.7	54
50_3	Jiaojia	JJ3	700.00	11.0	13.50	366.00	18.4	16.5	0.01	75.4	6360.0	0.09	3	0.1	358.00	3.4	1
50_4	Jiaojia	JJ3	501.00	20.4	77.40	296.00	12.6	9.7	0.01	28.4	3330.0	0.10	5	0.1	241.00	0.4	1
50_5	Jiaojia	JJ3	180.00	45.4	243.00	68.10	6.8	10.1	0.01	26.0	1360.0	0.09	3	0.1	58.60	0.3	1
50_6	Jiaojia	JJ3	310.00	19.1	559.00	137.00	8.2	14.1	0.01	19.9	1760.0	0.11	5	0.1	108.50	0.2	1
50_7	Jiaojia	JJ3	290.00	16.3	160.00	171.00	18.3	16.0	0.01	26.0	3260.0	0.08	4	0.1	138.00	7.7	13
1_2	Xincheng	X1	190.00	144.5	126.00	14.15	4.2	4210.0	1.08	14.9	1560.0	6.61	2	0.9	6.55	1.3	47
2_1	Xincheng	X1	120.00	142.5	26.70	51.20	99.3	56.3	1.56	60.0	3580.0	1.94	2	0.9	42.30	3.0	34
5_2	Xincheng	X1	11.90	60.1	14.40	33.30	39.7	18.4	0.25	23.7	126.5	0.85	6	0.1	16.45	0.6	1
6_4	Xincheng	X1	69.80	75.1	142.00	65.50	53.4	24.9	0.13	23.6	916.0	1.31	5	0.2	29.40	0.7	3
8_1_1	Xincheng	X1	150.00	67.9	120.00	51.30	3.9	51.2	0.50	11.8	1920.0	1.19	5	0.3	35.30	6.2	167
8_1_2	Xincheng	X1	4.98	179.5	4.10	8.23	2.4	15.8	0.08	8.1	159.5	0.95	4	0.1	7.89	1.8	3
8_1_3	Xincheng	X1	4.90	92.7	0.90	12.25	3.4	33.7	0.19	10.3	185.5	1.93	4	0.2	9.41	2.2	17
9_4	Xincheng	X1	3.86	87.3	0.20	11.65	9.4	11.6	0.07	28.0	399.0	1.22	2	0.1	4.28	2.6	9
9_5	Xincheng	X1	10.80	135.0	4.80	17.45	14.9	27.8	0.08	65.0	668.0	3.31	3	0.4	9.09	3.6	71
9_7	Xincheng	X1	15.65	359.0	9.80	28.20	9.6	36.4	0.08	129.5	660.0	1.48	3	0.2	9.26	16.9	1
52_10	Xincheng	X1	19.10	56.7	114.00	367.00	25.1	32.5	0.14	12.4	178.5	1.02	5	0.1	224.00	0.5	1
52_13	Xincheng	X1	360.00	42.4	2720.00	418.00	5.4	22.1	0.08	1.7	205.0	0.25	4	0.1	249.00	0.1	1
89_1	Xincheng	X1	21.30	64.9	17.30	39.80	70.7	6.2	0.09	69.4	43.6	0.15	4	0.1	26.30	2.7	1

of pyrite samples with galena, which in the JJ3 orebody is documented to contain several wt.% Ag (Mills et al., in review-a). However, sulfide petrography does not support the existence of more galena inclusions in the JJ3 pyrites, with galena occurring as a discrete mineral separate from pyrite. Hand-picking of pyrite separates included visual screening to remove any visibly contaminated pyrite crystals. As all JJ1, X1, and JJ3 samples were picked during the same process, it is highly unlikely that only JJ3 crystals would be contaminated by galena. Additionally, this explanation does not account for the slightly higher Ag content in electrum in the JJ3 orebody, the overall higher abundance of galena in the JJ3 orebody relative to the JJ1 and X1 orebodies, or why preferential Ag and Pb enrichment in individual ore deposits is observed in studies of other deposits in the Jiaodong district (to be discussed in Section 5.1). As such, although some of the correlations observed may be influenced by minor galena inclusions in pyrite, the Ag and Pb enrichment is interpreted to be a valid geochemical anomaly.

4.1.3. In situ pyrite geochemistry

The results of the in situ pyrite analyses are presented in Appendix A1. The laser ablation ICP-MS transects across JJ3 pyrite crystals illustrate that there is a considerable trace element variation within and between individual pyrite crystals. There is good agreement in the trends between Ag, Pb, Bi, and Te (Fig. 8C). The trends between Ag and Au, as well as Au and As, are less well defined. Within individual crystals, Au appears well correlated with As at some peaks, well correlated with Ag at others, and in some cases all 3 elements appear to have related peaks (Fig. 9). Where Au is correlated with Ag, it is typically a sign of electrum particles, which is supported by petrographic observations. Where Au correlates with As, it is typically a sign of 'invisible gold', which forms as solid solution in As-rich pyrite and has been documented as a minor gold-bearing phase in the Xincheng and Jiaojia deposits (Cook and Chryssoulis, 1990; Reich et al., 2005; Mills et al., in review-b). However, the distinct peaks in the laser ablation transects
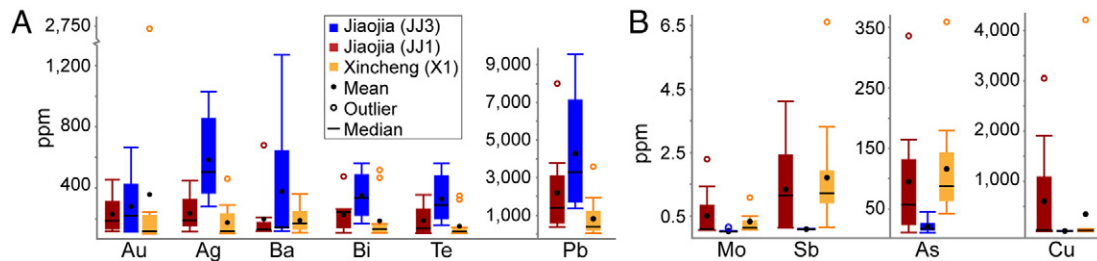
Fig. 6. Comparative box plot of bulk pyrite geochemistry from the JJ1, X1, and JJ3 orebodies, illustrating the concentration range of particular elements in each orebody and highlighting significant relative enrichments. Boxes represent interquartile range (data between 25th and 75th percentiles), with top and bottom lines extending 1.5 times the interquartile range towards the maximum and minimum. Hollow circles represent outliers greater than 1.5 times the interquartile range. Plot based on 9 points for the JJ1 orebody, 11 points from the X1 orebody, and 6 points from the JJ3 orebody.
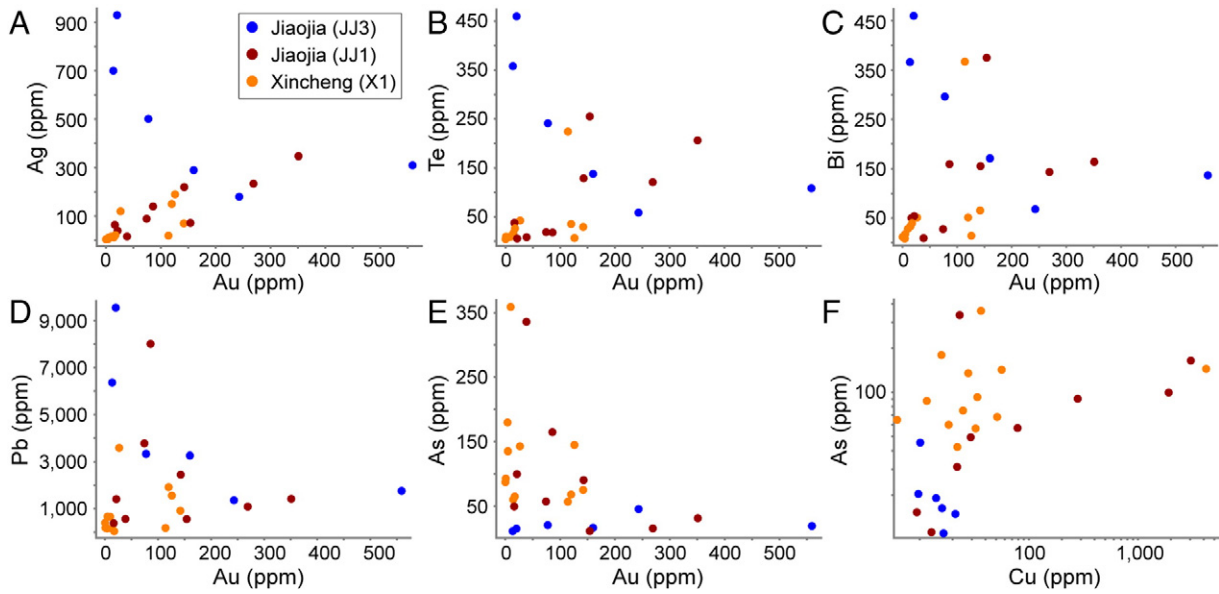
Fig. 7. Results of bulk pyrite geochemistry illustrating the variations in element correlations between different orebodies. For the JJ3 orebody the negative correlation between Au and Ag is markedly different from the positive relationship for JJ1 and X1. Negative correlations for JJ3 are also found between Au and Te, Bi and Pb as shown in A, B, C, and D. E and F show the substantially lower As and Cu concentrations in JJ3.

are more indicative of mineral inclusions than solid-solution. Considering this, it is possible that there has been remobilisation of solid solution As and Au within the pyrite grains (Cook et al., 2013).

4.1.4. Sulfur isotopes

The sulfur isotope data for pyrites from the JJ3 orebody (Table 2) are within the range of the sulfur isotope signature of JJ1 and X1 pyrites. The JJ3 results are at the higher end of the $\delta^{34}S$ spectrum for the Jiaodong district, with JJ1 and X1 results ranging from 8–13‰, averaging 10.41‰, whereas JJ3 results range from 10–13‰ and average 11.42‰ (Fig. 10).
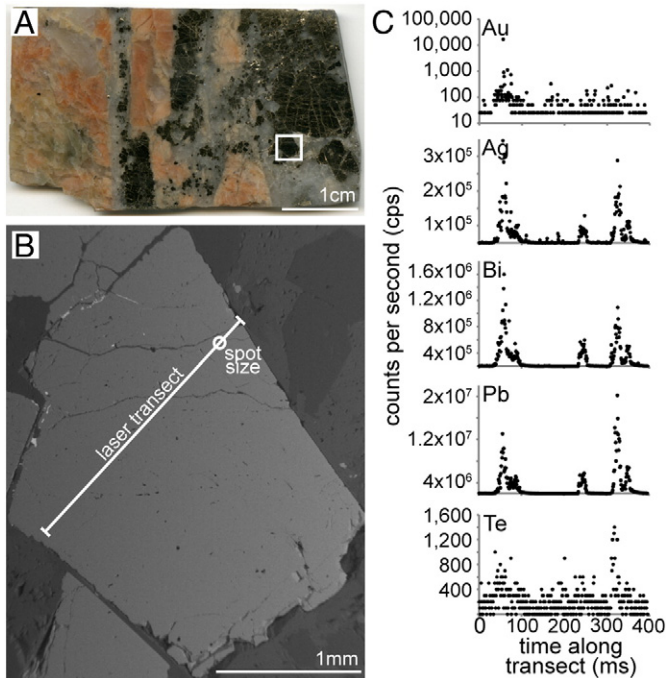
Fig. 8. Results from laser transect across sample 50-5, crystal 2 from the JJ3 orebody. (A) Polished block of sample 50-5 used for analyses. Notice the red tint in the wallrock related to K-feldspathic alteration, as well as the sharp contact between wallrock and quartz-pyrite vein. (B) BSE SEM image of crystal 2 with the location of the transect and an indication of laser spot size used. (C) Results of the laser transect. The x-axis represents time as the laser moves across the crystal (proxy for distance), and the y-axis represents the counts-per-second values for each element, taken as the relative concentration of each element in pyrite. Only results from measurements in the pyrite crystal are included, with results from laser warm-up, wash-out, and the silicate matrix removed.
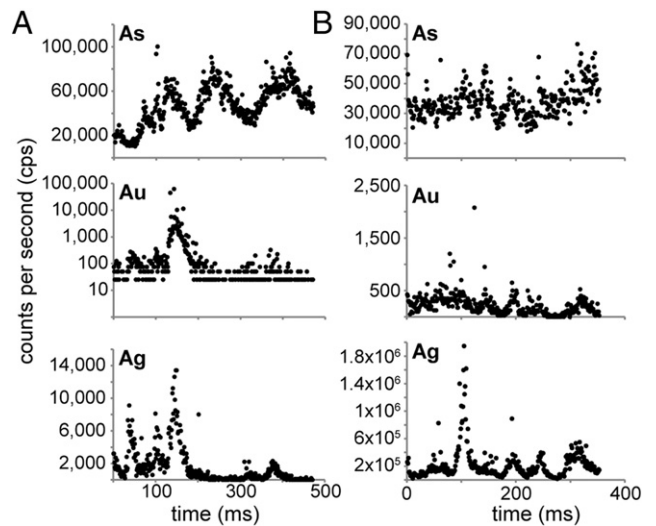
Fig. 9. Relative As, Ag, and Au variations along a laser transect across two pyrite crystals from the JJ3 orebody. The x-axis represents time as the laser moves across the crystal (proxy for distance), and the y-axis represents the counts-per-second values for each element. Only results from measurements in the pyrite crystal are included, with results from laser warm-up, wash-out, and the silicate matrix removed. These figures illustrate in situ element variations in single pyrite crystals. (A) Au and Ag appear correlated along most peaks, with a major Au–Ag peak also in good agreement with an As peak. However, a minor Au–Ag peak around 375 ms is not as well correlated with As, and an early peak ~50 ms for Au and Ag corresponds to a trough in As data (results from sample 50-6, crystal 4). (B) A large Ag peak around 100 ms has little correlation in Au and As. However, a later Ag peak around 200 ms is in good agreement with Au and As, and a final peak around 310 ms is only represented in Au and Ag (results from sample 50-6, crystal 2).

Table 2
Sulfur Isotopes of pyrite from the JJ1, JJ3 and X1 orebodies.

Sample	Deposit	Orebody	$\delta^{34}S$ (‰)	Sample	Deposit	Orebody	$\delta^{34}S$ (‰)
1 2	Xincheng	X1	10.95	50 1	Jiaojia	JJ3	10.26
2 1	Xincheng	X1	10.71	50 3	Jiaojia	JJ3	11.82
8 1 1	Xincheng	X1	9.69	50 4	Jiaojia	JJ3	12.72
8 1 2	Xincheng	X1	12.38	50 5	Jiaojia	JJ3	10.47
8 1 3	Xincheng	X1	8.92	50 6	Jiaojia	JJ3	11.16
9 4	Xincheng	X1	12.22	50 7	Jiaojia	JJ3	12.09
9 5	Xincheng	X1	10.88				
9 7	Xincheng	X1	8.70				
52 10	Xincheng	X1	11.38				
89 1	Xincheng	X1	10.83				
3 1	Xincheng	X1	8.33				
5 1 1	Xincheng	X1	11.29				
5 1 2	Xincheng	X1	8.74				
6 2	Xincheng	X1	10.94				
14 1	Jiaojia	JJ1	10.65				
43 2	Jiaojia	JJ1	11.74				
49 4	Jiaojia	JJ1	11.29				
10 2	Jiaojia	JJ1	8.48				
11 1	Jiaojia	JJ1	8.68				
43 1	Jiaojia	JJ1	10.63				
51 6	Jiaojia	JJ1	12.71				
51 7	Jiaojia	JJ1	8.82				
78 2	Jiaojia	JJ1	11.00				

4.2. Whole-rock geochemistry

Major, trace, and rare earth element (REE) analyses were conducted on altered whole-rock samples from JJ3 (n = 6), JJ1 (n = 17), and X1 (n = 29) to compare the alteration signatures between different orebodies. Five unaltered samples of Guojialing granodiorite and five unaltered samples of Linglong granite were also analysed. Whole rock samples collected in the field were cleaned and crushed first in a ceramic jaw crusher, followed by pulverisation in an agate mill to a fine powder (<75 μm). These pulps were sent to ALS Laboratories for analyses. For REE and incompatible element analyses, a 0.1 g powder sample was added to 1.8 g lithium metaborate/lithium tetraborate ($LiBO_2$/$Li_2B_4O_7$) flux, mixed well, and fused in a furnace at 1025 °C. The resulting melt was cooled and dissolved in an acid mixture containing nitric, hydrochloric and hydrofluoric acids. This solution was analysed by ICP-MS. For major element oxides, 0.1 g powder sample is added to 0.9 g lithium metaborate/lithium tetraborate ($LiBO_2$/$Li_2B_4O_7$) flux, mixed well, and fused in a furnace at 1000 °C. The resulting melt was
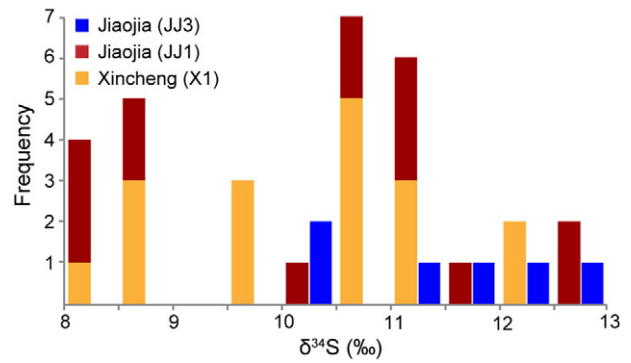
Fig. 10. Sulfur isotope results for the JJ3 orebody as compared to the JJ1 and X1 orebodies.

cooled and dissolved in 100 mL of 4% nitric acid and 2% hydrochloric acid. This solution was analysed by ICP-AES, with results corrected for spectral inter-element interferences. The precision of the data was not reported by ALS. Results are presented in Appendix A2.

The whole-rock geochemistry results indicate that all orebodies are generally depleted in Na and Ca and enriched in Si relative to the primary intrusions. The JJ3 samples show particular depletion in Fe and Mg and enrichment in K relative to JJ1 and X1 (Fig. 11), as expected from the primary breakdown of biotite (e.g. Fig. 4E).

Pearce element ratio (PER) diagrams (Fig. 12), the JJ3 samples exhibit slightly more affinity for K-feldspar end-members as opposed to mica-rich end-members. This is not unique to the JJ3 samples, as a number of samples from JJ1 and especially X1 orebodies also plot closer to K-feldspar compositions, though K-feldspar affinity is particularly well developed in the JJ3 samples. More JJ1 samples appear to have developed significant muscovite through loss of Ca and Na compared to both JJ3 and X1. There is no evidence for sodic alteration or development of extensive clay minerals in any of the orebodies. Alteration appears to follow a relatively simple trend from unaltered granitic compositions to K-feldspathisation before being increasingly overprinted by sericitisation (Fig. 12). There is a minor chlorite signature apparent in some samples, conspicuously absent from JJ3 samples, likely related to development of small amounts of chlorite in the brecciated zone proximal to the JJ-X fault.

The REE patterns for the different orebodies illustrate, particularly in the JJ3 and X1 samples, that there is a relative depletion of LREE
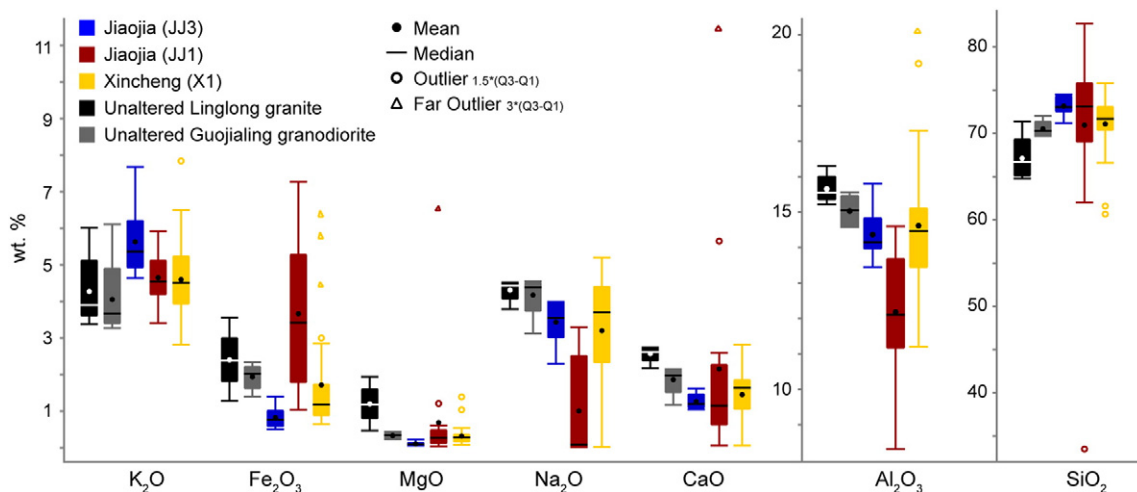
Fig. 11. Comparative box plot of whole-rock geochemistry from the JJ1, X1 and JJ3 orebodies as well as the Linglong and Guojialing intrusions illustrating the concentration range of particular elements in each orebody and highlighting significant relative enrichments. Boxes represent interquartile range (data between 25th and 75th percentiles), with top and bottom lines extending 1.5 times the interquartile range towards the maximum and minimum. Plot based on 17 samples for JJ1, 29 samples for X1, 6 samples for JJ3, and five samples each for the Linglong and Guojialing.

Fig. 12. Pearce element ratio (PER) diagrams illustrating the two stages of alteration in the Jiaojia and Xincheng deposits. Arrow 1 indicates early K-feldspathisation of granitoid compositions, whereas Arrow 2 shows the trend towards (A) sericitic and (C) chloritic alteration assemblages, at the expense of Ca and Na (B).
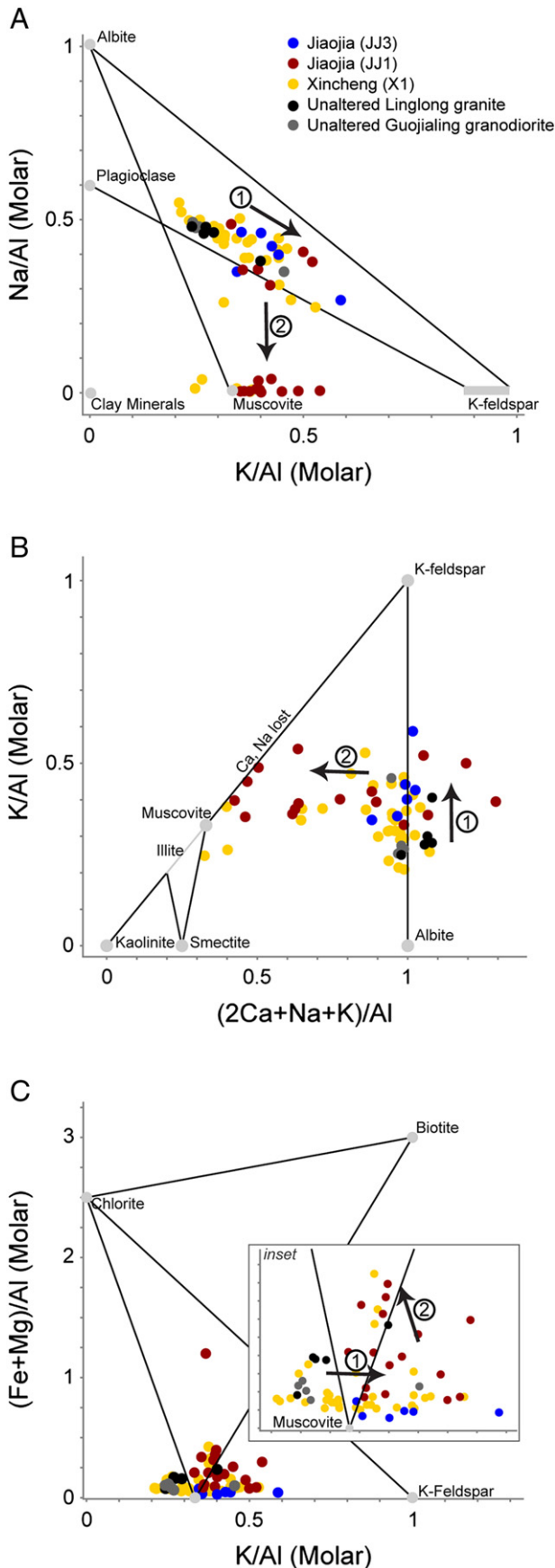
compared to the original unaltered host rock (Fig. 13). In the JJ3 samples particularly, the depletion in LREE has given the HREE a flat to slightly positive slope, though actual enrichment of HREE appears to be negligible. One sample in the JJ3 suite, which is defined by the dark blue line in Fig. 13, shows a significant increase in HREE relative to the Linglong granite. In general, there is a higher degree of variability in the REE results than is typically expected for gold-related alteration. The values are likely influenced by the composition of the original granitoids, which exhibit cumulate, schlieren, enclave, and magmatic flow textures. This is particularly an issue in the Guojialing granodiorite, as the abundance of REE-controlling minerals such as hornblende, titanite, and biotite is widely variable on a ten-to-hundred metre scale.

5. Discussion

5.1. Geochemical constraints on hydrothermal fluids

5.1.1. Ore-forming fluids

Concentrations of up to 30% Ag in electrum are common in many deposits of the Jiaodong district, and Ag is produced as a by-product in the Linglong gold mine. As such, the presence of Ag in Au deposits around the Jiaodong district is not a remarkable phenomenon, and has been noted by previous pyrite geochemistry studies of deposits in the Jiaodong district (e.g. Yan et al., in press; Yang et al., 2013). However, preferential Ag (and Pb) enrichment within a deposit, as exhibited by the JJ3 orebody in comparison with the JJ1 orebody, has been documented in only one other deposit in the Jiaodong district (Yang et al., 2009; L.-Q. Yang et al., 2014), making it a unique event within the Jiaodong district. Additionally, the Cu-poor nature of the JJ3 pyrites is distinct, since studies such as Li et al. (2004) note that the JJ1 orebody is more enriched in Cu relative to other base metals. Copper is also an important trace element in pyrite in other areas of the Jiaodong district; for example, the Jinqingding deposit in the east of the Jiaodong district contains economic Cu concentrations in shallow levels of the deposit. As such, the combined Ag and Pb enrichments and Cu depletion in the JJ3 orebody are noteworthy and likely indicate that there were multiple stages in the mineralisation history of the Jiaojia deposit as a whole.

In the only other Jiaodong deposit known to exhibit anomalous Ag enrichment, the Dayingezhuang deposit, mineralisation is dominantly disseminated/veinlet style and is hosted in Linglong granite along the footwall of the SE dipping Zhaoping fault (Fig. 1). Although it is noted that quartz-sulfide veins are locally developed in Dayingezhuang, the size, location, and orientation of these veins are not discussed (Yang et al., 2009). The No. 1 orebody of the Dayingezhuang deposit is enriched in Ag, which is interpreted to be the result of a late overprinting event (Yang et al., 2009), whereas the No. 2 orebody is not, although they both exhibit the same mineralisation style. The Ag content in the No. 1 orebody increases with depth, from ~2 ppm at shallow levels to 50 ppm over a 250 m depth interval (Yang et al., 2009). It is unclear from this study whether there are any overgrowth textures to support the interpretation of a 'late' overprint, although there is a suite of Ag minerals documented (e.g. native Ag, kuestelite, hessite, argentite, acanthite, polybasite, and pearceite; L.-Q. Yang et al., 2014). In the JJ3 orebody, Ag is mostly contained in electrum, argentiferous galena, and hessite and only overprints pyrite, appearing generally contemporaneous with similar precious metal phases. Silver mineralisation at Dayingezhuang is observed to occur with galena, sphalerite, barite, and calcite (L.-Q. Yang et al., 2014). Although significant sphalerite is not observed in JJ3, galena and barite are both more abundant in JJ3 than in JJ1 and X1. Calcite is common, though not necessarily more so
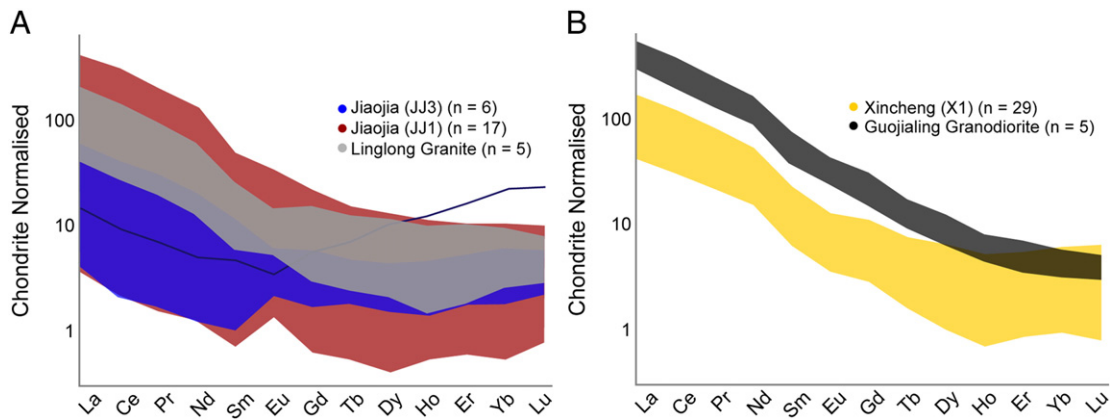
Fig. 13. Chondrite normalised REE spider diagram (after McDonough and Sun, 1995) for (A) unaltered Linglong and altered Linglong from the Jiaojia deposit, and for (B) unaltered Guojialing and altered Guojialing from the Xincheng deposit. The dark blue line in (A) represents an anomalously HREE enriched sample from the JJ3 suite.

than in JJ1 and X1. Thus, the nature of Ag mineralisation at JJ3 and Dayingezhuang is similar.

Fluid inclusion studies from the Dayingezhuang deposit propose that early hydrothermal fluids were originally K_2SO_4 type, later evolving to NaCl type fluids (Yang et al., 2009). However, L.-Q. Yang et al. (2014) found no obvious reason for the Ag enrichment. An evolution to more saline fluids for the Ag-enrichment event is in agreement with the geochemical data in L.-Q. Yang et al. (2014), because Ag and Pb are effectively transported in hydrothermal fluids as chloride complexes (Large, 1992). However, if this was the case, Cu content would be elevated rather than the low contents observed in the JJ3 orebody, since Cu is also effectively transported in chloride complexes (Liu and McPhail, 2005). A likely explanation for the observed metal association relates to hydrothermal fluid temperature variations, similar to those that cause metal zonations in VMS and SEDEX deposits (e.g. Barnes, 1975). Lead and Ag are more soluble in chloride complexes at lower temperatures than Cu, as is Au in bisulfide complexes (Hayashi and Ohmoto, 1991; Large, 1992). The difference in solubility at lower temperatures means that Ag, Pb and Au can travel farther from the source of heat driving a hydrothermal system before precipitating than Cu. The lack of Cu and abundance of Ag and Pb in the JJ3 ores suggest that a cooler fluid was responsible for this mineralisation. Fluid inclusion studies of Jiaojia- and Linglong-style deposits in the Jiaodong district generally indicate ore-forming fluids of moderate to low salinity at 200–350 °C (e.g. Fan et al., 2007; Z.-L. Wang et al., 2015), however there appears to be no study differentiating between fluid inclusions from the JJ1 and JJ3 orebodies that would allow further evaluation of our hypothesis.

The presence of barite in both the JJ3 orebody and the No. 1 orebody in Dayingezhuang can be explained in two ways: 1) evolution of the magmatic–hydrothermal fluid to more oxidising conditions (Mills et al., in review-a), or 2) mixing of the magmatic–hydrothermal fluid with seawater. In Mills et al. (in review-a), the paragenetic sequence for the Jiaojia, Xincheng, and Jiuqu (of the Linglong gold field) deposits was determined to represent the evolution of a magmatic hydrothermal fluid from reducing conditions associated with pyrite precipitation to oxidising conditions associated with iron oxide and sulfate mineral precipitation, including barite. This evolution is considered to be intrinsic in the magmatic–hydrothermal system, relating to early removal of ferrous iron from the magma causing 'self-oxidation' of both the magma and progressively exsolved fluids (Bell and Simon, 2011). In this context, barite is a paragenetically late phase. Furthermore, given that the $\delta^{34}S$ values of magmatic–hydrothermal fluids increase with an increasingly oxidised magmatic source (Zheng, 1990), the slightly higher $\delta^{34}S$ values in the JJ3 orebody can be explained by mineralisation from a late oxidised magmatic–hydrothermal fluid.

Alternatively, mixing between seawater (~20‰) and magmatic hydrothermal fluids, through normal faulting and draw-down of shallow fluids into a convecting hydrothermal system (e.g. Rowland and Sibson, 2004), provides a high-$\delta^{34}S$ end-member that may account for the values observed in Jiaodong. In a seawater mixing scenario, the presence of barite (and calcite) is explained through processes similar to those producing white smokers on the sea-floor, which form during the interaction between hot magmatic–hydrothermal fluids and cold seawater (de Ronde et al., 2003). However, the lack of Paleozoic to late Mesozoic strata in the Jiaodong district makes it difficult to assess the possibility of marine input into the Cretaceous Jiaodong hydrothermal system. Shallow marine strata of Cambrian and Permian age in western Shandong province and in the Liaoning peninsula across the Bohai Sea indicate the past existence of a shallow sea over east China (Lee and Chough, 2011). However, the Jiaolai Basin in the Jiaodong district, which opened in the late Cretaceous after peak mineralisation, is comprised of mainly lacustrine and alluvial sediments (L. Zhang et al., 2003). Consequently, it is unclear whether a source for seawater was available to the Jiaodong district during mineralisation.

In this study we favour explanation of barite and high-$\delta^{34}S$ values through progressive magmatic oxidation due to the ambiguous nature of the Cretaceous sea-level in Jiaodong. Barite resulting from evolved magmatic–hydrothermal fluids is in agreement with Ag and Pb enrichment in a cooler fluid, as both would be part of a relatively late mineralising event in the JJ3 orebody.

5.1.2. Whole-rock geochemistry

The whole-rock geochemistry results for the Jiaojia and Xincheng deposits are in good agreement with a study of the hydrothermal alteration in the nearby Sanshandao deposit (Li et al., 2013). This deposit lies 15 km to the west of the Jiaojia-Xincheng camp and is hosted along the NE striking, NW dipping Sanshandao-Cangshang fault. In the Sanshandao deposit, the paragenetic alteration sequence was also defined as early K-feldspar alteration overprinted by sericitic + silicic alteration, with a later ore-bearing stage of sericitic + silicic + pyritic alteration (Li et al., 2013). One of the most striking similarities between the whole-rock geochemistry of the Jiaojia-Xincheng and Sanshandao deposits is the LREE depletion and resulting flat-to-positive HREE slope found in the JJ3 samples of the JJ-X camp (Fig. 13) and in the K-feldspar alteration suite of the Sanshandao deposit (Li et al., 2013). As shown in Fig. 12, the JJ3 samples represent K-feldspar alteration with negligible sericitic overprint, whereas the JJ1 and X1 suites include a mixture of K-feldspar and sericite altered samples. As such, the JJ3 samples are the best direct comparison to the K-feldspar alteration suite of samples in Li et al. (2013), so the unique REE trend appears to be a distinct feature of the K-feldspar alteration stage.

The Linglong granite, host rock to both the K-feldspar alteration suite of samples from Li et al. (2013) and the JJ3 samples, is a monzogranite primarily comprised of feldspar and quartz. It also contains minor biotite and hornblende along with zircon, titanite, apatite, magnetite, and garnet as accessory phases, the formation and breakdown of which can have significant impact on REE distribution and mobilisation. Additionally, it has been well-documented that REE can be fluid-mobilised in some magmatic–hydrothermal systems (e.g. Salvi and Williams-Jones, 1996; van Dongen et al., 2010) where hot oxidising fluids contain abundant chloride, fluoride, or sulfate complexes available as ligands (Hetherington et al., 2010; van Dongen et al., 2010; Williams-Jones et al., 2012).

As illustrated in Fig. 4e, biotite is destroyed as K-feldspar alteration progresses. As biotite can host significant LREE (Nash and Crecraft, 1985), it is likely that the breakdown of biotite is one of the main causes of the LREE depletion observed. The breakdown of biotite is also in agreement with the distinct Fe- and Mg-depleted major element signature of the JJ3 alteration. As zircon and garnet are favourable hosts for HREE (Irving and Frey, 1978), it is possible that residual magmatic phases or the introduction of hydrothermal phases of these minerals accounts for the anomalously HREE-enriched sample in the JJ3 suite (Fig. 13). From a hydrothermal fluid perspective, LREE are expected to be more mobile than HREE in hydrothermal solution, such as at the Nechalacho REE deposit, where LREE were mobilised far greater distances than HREE (Williams-Jones et al., 2012). In the Jiaodong district, the primary ore-forming fluids are not likely to have been significantly oxidising or chloride/fluoride-rich (Fan et al., 2003; Li et al., 2013; Yang et al., 2009). However, K-feldspathic alteration is an earlier fluid event than ore-formation and is likely to have been the hottest hydrothermal fluid phase interacting with the country rock (Plümper and Putnis, 2009) and therefore may have been able to preferentially mobilise and strip LREE from the country rock, contributing to the observed LREE depletion trend. Since the LREE depletion appears most significant in the K-feldspathic alteration phase, the combination of primary biotite breakdown and LREE mobility in hot hydrothermal fluids can explain the LREE depletion, though further investigation of magmatic and hydrothermal REE minerals and hydrothermal REE transport is needed to fully understand the trends observed in this study and in Li et al. (2013).

There is no evidence that infiltration of mineralising fluids into the dilational veins of the JJ3 orebody had a significant effect on the host rock since there is no apparent preferential alteration in the host rock around the veins, even on a centimetre to millimetre scale. This lack of directly associated alteration is consistent with an extensional setting where the pressure gradient is towards the dilational veins, given that high fluid pressures would be required to push fluids into the impermeable granitic host rocks. Therefore, it is likely that the alteration signature of the JJ3 orebody is due to an earlier, high temperature fluid flux, and is geochemically disconnected from the lower temperature mineralisation. As a result, geochemical exploration based on alteration vectors for similar orebodies is unlikely to prove effective.

5.2. Orebody structure

Extensional tectonism in the Jiaodong district is thought to have initiated as early as 160–150 Ma, with exhumation of the Linglong granite from 143–134 Ma, followed by brittle faulting (Charles et al., 2013; Lu et al., 2007). Cessation of brittle deformation has been dated at 128 Ma by ^{40}Ar–^{39}Ar dating of sericite from the Zhaoping fault at the south-eastern margin of the Linglong granite (Charles et al., 2013). The Guojialing granodiorite exhibits evidence for ductile deformation, indicating emplacement as a syn-kinematic pluton in the upper crust (Charles et al., 2011b). The well-developed fabric in this intrusion indicates that extension was still active at 125 Ma. Late Cretaceous granites such as the Aishan, which intruded the northern portion of the Linglong

granite, and the Weideshan and Haiyang granites, which are located in the east of the Jiaodong district, were intruded at 120–118 Ma (Charles et al., 2011a; Goss et al., 2010). These granites are undeformed (Charles et al., 2011a) and hence effectively bracket the end of the Jiaodong extensional event to roughly between 125 and 120 Ma, overlapping with the timing of the majority of mineralisation in the region.

The varied structural styles of mineralisation in the Jiaojia-Xincheng field indicate that deformation related to the intrusion of the Guojialing granodiorite developed in multiple ways. Intense normal movement and brecciation along the regional JJ-X fault favoured formation of the main JJ1 and X orebodies, whereas the JJ3 orebody formed through the opening of tensile cracks parallel to σ_1. Considering that mineralisation in the JJ3 orebody is interpreted to be a later event than the mineralisation in the JJ1 and X1 orebodies, and that mineralisation hosted in dilational structures is contemporaneous with the formation of such structures, the development of extension fractures appears to be a final stage in the brittle deformation of the Jiaojia-Xincheng field.

6. Future exploration and conclusions

The structural setting and significant Ag and Au endowment of the JJ3 orebody make this style of mineralisation an important target for future exploration in the Jiaodong district and highlights the need to consider multiple styles of mineralisation within one deposit. The abundance of argentiferous galena and barite in the JJ3 orebody, resulting in Ag, Pb, and Bi enrichment in ore-zone pyrites, indicate that Ba and Pb are likely to be the most useful geochemical pathfinder elements. The lack of chalcopyrite and relative depletion of As in pyrite make Cu and As a poor choice for exploration, despite the usefulness of As in other gold districts worldwide, such as the Yilgarn Craton in Australia. Major element trends are likely to be of use for exploration, if a reliable baseline can be established, due to the wide alteration halo and major element discrimination between different orebodies, with JJ3 exhibiting slightly more K-enriched and Fe- and Mg-depleted signatures characteristic of the dominant K-feldspar alteration. However, considering that alteration surrounding the JJ3 veins is interpreted to reflect an earlier event, structural targeting is likely to be a more effective method for locating JJ3-like deposits than using alteration as an indicator of mineralisation. Since formation of the JJ3 orebody was controlled by normal faulting, there is no reason it should be a phenomenon restricted to the Linglong granite or the JJ-X fault. This style of mineralisation could form adjacent to other regional faults that were active under extensional tectonics, such as the Sanshandao-Cangshang fault and the southern portion of the Zhaoping fault. Depending on the depth of certain deposits during mineralisation, it is also possible that the JJ3 orebody extends deeper than the current level it is mined to, as tension gashes should develop throughout the brittle deformation zone.

Appendix A. Supplementary data

Supplementary data to this article can be found online at http://dx. doi.org/10.1016/j.oregeorev.2014.12.014.

References

Barnes, H.L., 1975. Zoning of ore deposits: types and causes. Trans. R. Soc. Edinb. Earth Environ. Sci. 69, 295–311.

Bell, A.S., Simon, A., 2011. Experimental evidence for the alteration of the $Fe^{3+}/\Sigma Fe$ of silicate melt caused by the degassing of chlorine-bearing aqueous volatiles. Geology 39, 499–502.

Cai, Y.C., Fan, H.R., Santosh, M., Liu, X., Hu, F.F., Yang, K.F., Lan, T.G., Yang, Y.H., Liu, Y., 2013. Evolution of the lithospheric mantle beneath the southeastern North China Craton: Constraints from mafic dikes in the Jiaobei terrain. Gondwana Res. 24, 601–621.

Charles, N., Chen, Y., Augier, R., Gumiaux, C., Lin, W., Faure, M., Monié, P., Choulet, F., Wu, F., Zhu, R., Wang, Q., 2011a. Palaeomagnetic constraints from granodioritic plutons (Jiaodong Peninsula): new insights on Late Mesozoic continental extension in Eastern Asia. Phys. Earth Planet. Inter. 187, 276–291.

Charles, N., Gumiaux, C., Augier, R., Chen, Y., Zhu, R., Lin, W., 2011b. Metamorphic core complexes vs. synkinematic plutons in continental extension setting: insights from key structures (Shandong Province, eastern China). J. Asian Earth Sci. 40, 261–278.

Charles, N., Augier, R., Gumiaux, C., Monié, P., Chen, Y., Faure, M., Zhu, R., 2013. Timing, duration and role of magmatism in wide rift systems: insights from the Jiaodong Peninsula (China, East Asia). Gondwana Res. 24, 412–428.

Cook, N.J., Chryssoulis, S.L., 1990. Concentrations of invisible gold in the common sulfides. Can. Mineral. 28, 1–16.

Cook, N.J., Ciobanu, C.L., Meria, D., Silcock, D., Wade, B., 2013. Arsenopyrite–pyrite association in an orogenic gold ore: tracing mineralization history from textures and trace elements. Econ. Geol. 108, 1273–1283.

de Ronde, C.E.J., Faure, K., Bray, C.J., Chappell, D.A., Wright, I.C., 2003. Hydrothermal fluids associated with seafloor mineralization at two southern Kermadec arc volcanoes, offshore New Zealand. Mineral. Deposita 38, 217–233.

Fan, H.R., Zhai, M.G., Xie, Y.H., Yang, J.H., 2003. Ore-forming fluid associated with granite-hosted gold mineralization at the Sanshandao Deposit, Jiaodong gold province, China. Mineral. Deposita 38, 739–750.

Fan, H.R., Hu, F.F., Yang, J.H., Zhai, M.G., 2007. Fluid evolution and large-scale gold metallogeny during Mesozoic tectonic transition in the Jiaodong Peninsula, eastern China. Geol. Soc. Lond. Spec. Publ. 280, 303–316.

Goldfarb, R.J., Taylor, R.D., Collins, G.S., Goryachev, N.A., Orlandini, O.F., 2014. Phanerozoic continental growth and gold metallogeny of Asia. Gondwana Res. 25, 48–102.

Goss, S.C., Wilde, S.A., Wu, F., Yang, J., 2010. The age, isotopic signature and significance of the youngest Mesozoic granitoids in the Jiaodong Terrane, Shandong Province, North China Craton. Lithos 120, 309–326.

Griffin, W.L., Andi, Z., O'Reilly, S.Y., Ryan, C.G., 1998. Phanerozoic evolution of the lithosphere beneath the Sino-Korean Craton. In: Flower, M.F.J. (Ed.), Mantle Dynamics and Plate Interactions in East Asia, American Geophysical Union, pp. 107–126.

Guo, P., Santosh, M., Li, S., 2013. Geodynamics of gold metallogeny in the Shandong Province, NE China: an integrated geological, geophysical and geochemical perspective. Gondwana Res. 24, 1172–1202.

Hacker, B.R., Wallis, S.R., Ratschbacher, L., Grove, M., Gehrels, G., 2006. High-temperature geochronology constraints on the tectonic history and architecture of the ultrahigh-pressure Dabie-Sulu Orogen. Tectonics 25.

Hayashi, K.I., Ohmoto, H., 1991. Solubility of gold in NaCl-and H_2S-bearing aqueous solutions at 250–350 °C. Geochim. Cosmochim. Acta 55, 2111–2126.

Hetherington, C.J., Harlov, D.E., Budzyń, B., 2010. Experimental metasomatism of monazite and xenotime: mineral stability, REE mobility and fluid composition. Mineral. Petrol. 99, 165–184.

Hou, M.L., Jiang, Y.H., Jiang, S.Y., Ling, H.F., Zhao, K.D., 2007. Contrasting origins of late Mesozoic adakitic granitoids from the northwestern Jiaodong Peninsula, east China: implications for crustal thickening to delamination. Geol. Mag. 144, 619–631.

Irving, A.J., Frey, F.A., 1978. Distribution of trace-elements between garnet megacrysts and host volcanic liquids of kimberlitic to rhyolitic composition. Geochim. Cosmochim. Acta 42, 771–787.

Jahn, B.M., Liu, D., Wan, Y., Song, B., Wu, J., 2008. Archean crustal evolution of the Jiaodong Peninsula, China, as revealed by zircon SHRIMP geochronology, elemental and Nd-isotope geochemistry. Am. J. Sci. 308, 232–269.

Large, R.R., 1992. Australian volcanic-hosted massive sulfide deposits: features, styles, and genetic models. Econ. Geol. 87, 471–510.

Large, R.R., Danyushevsky, L., Hollit, C., Maslennikov, V., Meffre, S., Gilbert, S., Bull, S., Scott, R., Emsbo, P., Thomas, H., Singh, B., Foster, J., 2009. Gold and trace element zonation in pyrite using a laser imaging technique: implications for the timing of gold in orogenic and carlin-style sediment-hosted deposits. Econ. Geol. 104, 635–668.

Lee, H.S., Chough, S.K., 2011. Depositional processes of the Zhushadong and Mantou formations (Early to Middle Cambrian), Shandong Province, China: Roles of archipelago and mixed carbonate-siliciclastic sedimentation on cycle genesis during initial flooding of the North China Platform. Sedimentology 58, 1530–1572.

Li, J.W., Vasconcelos, P., Zhang, J., Zhou, M.F., Zhang, X.J., Yang, F.H., 2003. $^{40}Ar/^{39}Ar$ constraints on a temporal link between gold mineralization, magmatism, and continental margin transtension in the Jiaodong Gold Province, eastern China. J. Geol. 111, 741–751.

Li, H., Shen, Y., Mao, J., Liu, T., Zhu, H., 2004. Features of trace elements in pyrite, quartz and their fluid inclusions: an example from Jiaojia-type gold deposits, northwestern Jiaodong Peninsula. Sci. Geol. Sin. 39, 320–328.

Li, J.W., Bi, S.J., Selby, D., Chen, L., Vasconcelos, P., Thiede, D., Zhou, M.F., Zhao, X.F., Li, Z.K., Qiu, H.N., 2012. Giant Mesozoic gold provinces related to the destruction of the North China Craton. Earth Planet. Sci. Lett. 349–350, 26–37.

Li, X.C., Fan, H.R., Santosh, M., Hu, F.F., Yang, K.F., Lan, T.G., 2013. Hydrothermal alteration associated with Mesozoic granite-hosted gold mineralization at the Sanshandao deposit, Jiaodong Gold Province, China. Ore Geol. Rev. 53, 403–421.

Li, L., Santosh, M., Li, S.-R., 2015. The 'Jiaodong type' gold deposits: characteristics, origin and prospecting. Ore Geol. Rev. 65, 589–611 (Part 3).

Liu, W., McPhail, D.C., 2005. Thermodynamic properties of copper chloride complexes and copper transport in magmatic–hydrothermal solutions. Chem. Geol. 221, 21–39.

Liu, J., Liu, F., Ding, Z., Yang, H., Liu, C., Liu, P., Xiao, L., Zhao, L., Geng, J., 2013. U-Pb dating and Hf isotope study of detrital zircons from the Zhifu Group, Jiaobei Terrane. North China Craton: Provenance and implications for Precambrian crustal growth and recycling. Precambrian Res. 235, 230–250.

Lu, H.Z., Archambault, G., Li, Y., Wei, J., 2007. Structural geochemistry of gold mineralization in the Linglong-Jiaojia district, Shandong Province, China. Chin. J. Geochem. 26, 215–234.

McDonough, W.F., Sun, S.S., 1995. The composition of the Earth. Chem. Geol. 120, 223–253.

Mills, S.E., Tomkins, A.G., Weinberg, R.F., Fan, H.R., 2014a. Gold precipitation linked to mineralogical priming in a progressively oxidizing magmatic–hydrothermal system, Jiaodong gold district, China. Econ. Geol. (in review-a).

Mills, S.E., Tomkins, A.G., Weinberg, R.F., Fan, H.R., 2014b. Implications of pyrite geochemistry for gold mineralisation and remobilisation in the Jiaodong gold district, northeast China. Ore Geol. Rev. (in review-b).

Nash, W.P., Crecraft, H.R., 1985. Partition coefficients for trace elements in silicic magmas. Geochim. Cosmochim. Acta 49, 309–322.

Plümper, O., Putnis, A., 2009. The complex hydrothermal history of granitic rocks: multiple feldspar replacement reactions under subsolidus conditions. J. Petrol. 50, 967–987.

Putnis, A., Hinrichs, R., Putnis, C.V., Golla-Schindler, U., Collins, L.G., 2007. Hematite in porous red-clouded feldspars: evidence of large-scale crustal fluid–rock interaction. Lithos 95, 10–18.

Qiu, Y., Groves, D.I., McNaughton, N.J., Wang, L.G., Zhou, T., 2002. Nature, age, and tectonic setting of granitoid-hosted, orogenic gold deposits of the Jiaodong Peninsula, eastern North China Craton, China. Mineral. Deposita 37, 283–305.

Reich, M., Kesler, S.E., Utsunomiya, S., Palenik, C.S., Chryssoulis, S.L., Ewing, R.C., 2005. Solubility of gold in arsenian pyrite. Geochim. Cosmochim. Acta 69, 2781–2796.

Rowland, J.V., Sibson, R.H., 2004. Structural controls on hydrothermal flow in a segmented rift system, Taupo Volcanic Zone, New Zealand. Geofluids 4, 259–283.

Salvi, S., Williams-Jones, A.E., 1996. The role of hydrothermal processes in concentrating high-field strength elements in the Strange Lake peralkaline complex, northeastern Canada. Geochim. Cosmochim. Acta 60, 1917–1932.

Song, M.-C., Li, S.-Z., Santosh, M., Zhao, S., Yu, S., Yi, P.-H., Cui, S.-X., Lv, G.-X., Xu, J.-X., Song, Y.-X., Zhou, M.-L., 2015. Types, characteristics and metallogenesis of gold deposits in the Jiaodong Peninsula, Eastern North China Craton. Ore Geol. Rev. 65, 612–625 (Part 3).

Tang, J., Zheng, Y.F., Wu, Y.B., Gong, B., Zha, X., Liu, X., 2008. Zircon U–Pb age and geochemical constraints on the tectonic affinity of the Jiaodong terrane in the Sulu orogen, China. Precambrian Res. 161, 389–418.

Van Dongen, M., Weinberg, R.F., Tomkins, A.G., 2010. REE-Y, Ti, and P remobilization in magmatic rocks by hydrothermal alteration during Cu–Au deposit formation. Econ. Geol. 105, 763–776.

Wang, L.G., Qiu, Y.M., McNaughton, N.J., Groves, D.I., Luo, Z.K., Huang, J.Z., Miao, L.C., Liu, Y.K., 1998. Constraints on crustal evolution and gold metallogeny in the northwestern Jiaodong Peninsula, China, from SHRIMP U–Pb zircon studies of granitoids. Ore Geol. Rev. 13, 275–291.

Wang, C., Deng, J., Santosh, M., Carranza, E.J.M., Gong, Q., Guo, C., Xia, R., Lai, X., 2015a. Timing, tectonic implications and genesis of gold mineralization in the Xincheng gold deposit, China: C–H–O isotopes, pyrite Rb–Sr and zircon fission track thermochronometry. Ore Geol. Rev. 65, 659–673 (Part 3).

Wang, Z.-L., Yang, L.-Q., Guo, L.-N., Marsh, E., Wang, J.-P., Liu, Y., Zhang, C., Li, R.-H., Zhang, L., Zheng, X.-L., Zhao, R.-X., 2015b. Fluid immiscibility and gold deposition in the Xincheng deposit, Jiaodong Peninsula, China: a fluid inclusion study. Ore Geol. Rev. 65, 701–717 (Part 3).

Williams-Jones, A.E., Migdisov, A.A., Samson, I.M., 2012. Hydrothermal mobilisation of the rare earth elements — a tale of "Ceria" and "Yttria". Elements 8, 355–360.

Wu, F.Y., Lin, J.Q., Wilde, S.A., Zhang, X., Yang, J.H., 2005. Nature and significance of the early Cretaceous giant igneous event in eastern China. Earth Planet. Sci. Lett. 233, 103–119.

Xiao, Y., Zhang, H.F., Fan, W.M., Ying, J.F., Zhang, J., Zhao, X.M., Su, B.X., 2010. Evolution of lithospheric mantle beneath the Tan-Lu fault zone, eastern North China Craton: evidence from petrology and geochemistry of peridotite xenoliths. Lithos 117, 229–246.

Yan, Y., Zhang, N., Li, S., Li, Y., 2013. Mineral chemistry and isotope geochemistry of pyrite from the Heilangou gold deposit, Jiaodong Peninsula, eastern China. Geosci. Front. (in press).

Yang, L.-Q., Deng, J., Guo, C., Zhang, J., Jiang, S., Gao, B., Gong, Q., Wang, Q., 2009. Ore-forming fluid characteristics of the Dayingezhuang gold deposit, Jiaodong gold province, China. Resour. Geol. 59, 181–193.

Yang, H.-Y., Wang, S.-H., Song, X.-L., Pan, H.-D., Ma, P.-C., 2011. Gold occurrence of Jiaojia gold mine in Shandong province. Trans. Nonferrous Metals Soc. China 21, 2072–2077.

Yang, K.F., Fan, H.R., Santosh, M., Hu, F.F., Wilde, S.A., Lan, T.G., Lu, L.N., Liu, Y.S., 2012. Reactivation of the Archean lower crust: Implications for zircon geochronology, elemental and Sr–Nd–Hf isotopic geochemistry of late Mesozoic granitoids from northwestern Jiaodong Terrane, the North China Craton. Lithos 146–147, 112–127.

Yang, Q., Shen, J., Li, S., Santosh, M., Luo, Z., Liu, Y., 2013. Oxygen, boron, chromium and niobium enrichment in native Au and Ag grains: A case study from the Linglong gold deposit, Jiaodong, eastern China. J. Asian Earth Sci. 62, 537–546.

Yang, L.-Q., Deng, J., Goldfarb, R.J., Zhang, J., Gao, B.-F., Wang, Z.-L., 2014a. $^{40}Ar/^{39}Ar$ geochronological constraints on the formation of the Dayingezhuang gold deposit: new implications for timing and duration of hydrothermal activity in the Jiaodong gold province, China. Gondwana Res. 25, 1469–1483.

Yang, Q., Santosh, M., Shen, J., Li, S., 2014b. Juvenile vs. recycled crust in NE China: Zircon U–Pb geochronology, Hf isotope and an integrated model for Mesozoic gold mineralization in the Jiaodong Peninsula. Gondwana Res. 25, 1445–1468.

Zhang, L., Shen, Y., Liu, T., Zeng, Q., Li, G., Li, H., 2003a. ^{40}Ar/^{39}Ar and Rb–Sr isochron dating of the gold deposits on northern margin of the Jiaolai Basin, Shandong, China. Sci. China Ser. D Earth Sci. 46, 708–718.

Zhang, X.O., Cawood, P., Wilde, S., Liu, R., Song, H., Li, W., Snee, L., 2003b. Geology and timing of mineralization at the Cangshang gold deposit, north-western Jiaodong Peninsula, China. Mineral. Deposita 38, 141–153.

Zhang, J., Zhao, Z.F., Zheng, Y.F., Dai, M., 2010. Postcollisional magmatism: Geochemical constraints on the petrogenesis of Mesozoic granitoids in the Sulu orogen, China. Lithos 119, 512–536.

Zheng, Y.F., 1990. Sulfur isotope fractionation in magmatic systems: models of Rayleigh distillation and selective flux. Chin. J. Geochem. 9, 27–45.

Zhu, R.X., Yang, J.H., Wu, F.Y., 2012. Timing of destruction of the North China Craton. Lithos 149, 51–60.